2019

An investigation into the prediction of double-skin penetration within chromite molds and cores in heavy section steel casting using process simulation software

Nathaniel Bryant
University of Northern Iowa

AN INVESTIGATION INTO THE PREDICTION OF DOUBLE-SKIN PENETRATION WITHIN CHROMITE MOLDS AND CORES IN HEAVY SECTION STEEL CASTING USING PROCESS SIMULATION SOFTWARE

An Abstract of a Thesis

Submitted

in Partial Fulfillment

of the Requirements for the Degree

Master of Science

Nathaniel Bryant

University of Northern Iowa

May 2019

ABSTRACT

This investigation was conducted in response to a commercial steel foundry approaching the University of Northern Iowa for assistance with a recurring defect they experienced on a production casting. The defect was described as a mass of metal that penetrated and consumed the interstices of their chromite molds and cores, and it was determined to consist of fayalite. After an extensive literature review, it was concluded that the foundry experienced the double-skin defect, a niche quality issue that most commonly occurs in heavy-section steel casting with chromite molding materials.

After it was determined that the double-skin defect was occurring, a methodology based on prior research was developed to understand the causation. Casting emissions data for the ester-cured phenolic resin system utilized by the commercial facility was collected to further understand the impact of mold atmosphere on double-skin penetration defects. High-temperature aggregate testing was also conducted to study the performance properties and characteristics of chromite sand with various levels of quartz contamination when exposed to temperatures seen in heavy-section steel casting.

The measured casting emissions data collected from the aforementioned ester-cured phenolic resin system matched data from prior research quite well, and exhibited a trend that coincided with an extrapolated version of the fayalite stability region. Utilizing the data collected, an algorithm was developed to predict the formation of double-skin penetration by means of the chemical penetration mechanism. Similarly, the results of the high-temperature aggregate testing provided the basis of the second proposed model,

which was developed to predict the same defect by the mechanical penetration mechanism.

Both models showed some level of agreement with the production casting, but it was determined that mechanical penetration was the principle mechanism for double-skin formation, as its associated algorithm predicted the defect more accurately than the version based on the chemical mechanism. The proposed models in their current state, however, could be used by commercial foundries within process simulation software packages to help make educated process and material decisions, and they are described in detail herein.

AN INVESTIGATION INTO THE PREDICTION OF DOUBLE-SKIN PENETRATION WITHIN CHROMITE MOLDS AND CORES IN HEAVY SECTION STEEL CASTING USING PROCESS SIMULATION SOFTWARE

A Thesis

Submitted

in Partial Fulfillment

of the Requirements for the Degree

Master of Science

Nathaniel Bryant

University of Northern Iowa

May 2019

This Study by: Nathaniel Bryant

Entitled: AN INVESTIGATION INTO THE PREDICTION OF DOUBLE-SKIN PENETRATION WITHIN CHROMITE MOLDS AND CORES IN HEAVY SECTION STEEL CASTING USING PROCESS SIMULATION SOFTWARE

has been approved as meeting the thesis requirement for the

Degree of Master of Science

_____	_____
Date	Dr. Scott Giese, Chair, Thesis Committee
_____	_____
Date	Dr. Joshua Sebree, Thesis Committee Member
_____	_____
Date	Dr. Zhe Zhang, Thesis Committee Member
_____	_____
Date	Dr. Jennifer Waldron, Dean, Graduate College

DEDICATION

This research is dedicated to my parents Erin Thiel & Keith Bryant, and my step-parents Jerry Thiel & Elise Bryant.

In addition, I'm dedicating this research to Elizabeth Zondo, the at-risk program coordinator at Union High School, who played a critical role in my educational career.

ACKNOWLEDGEMENTS

I would like to express my deepest gratitude to my thesis committee:

Scott Giese, PhD – Committee Chair

Zhe (Julie) Zhang, PhD – Committee Member

Joshua Sebree, PhD – Committee Member

I graciously appreciate the University of Northern Iowa Metal Casting Center staff for their assistance with this research.

Jerry Thiel	Travis Frush	Jiayi Wang
Sairam Ravi	Leah Dunlay	Kapil Gangwar

I received additional guidance from a variety of supporters from within the industry, namely:

Tyler Schneiter, Sivyer Steel Corporation
Keith Pearl, Sivyer Steel Corporation
Raymond Monroe, Steel Founders Society of America
Charlie Monroe, PhD, University of Alabama, Birmingham
Roy Stevenson, MAGMASoft
Joe Christensen, Emerson Process Management
Ayax Rangel, HA International
Amelia (Amy) Elliott, PhD, Oak Ridge National Laboratory

Last, but most certainly not least, I would like to acknowledge the effort put forth by my fellow student employees at the University of Northern Iowa Metal Casting Center.

Aaron Campbell	Landon Hinchman	Susan Alverio
Austin Knapp	Maria Alverio	Taite Gallagher
Bryon Sells	Mark McAllister	Taylor Clemons
Caitlyn Haller	Nathaniel Schmidt	Taylor Klein
Keelan Trent	Sarah Smithart	Yousef Almalki

TABLE OF CONTENTS

LIST OF TABLES

LIST OF FIGURES

FIGURE PAGE

DEFINITION OF TERMS

Equilibrium constant: Expresses the relationship between reactants and products of a specific reaction at equilibrium with relation to a specific unit. In this case, pressure.

Fugacity: The thermodynamic property that is used as a correction factor in equations for an ideal gas that, when substituted, gives results applicable to that of a real gas.

Gangue: The commercially valueless material in which ore is found.

Hematite: The mineral form of iron(III) oxide denoted by the chemical formula Fe_2O_3.

Kinetics: A branch of chemistry that is concerned mainly with the measurement and study of reaction rates.

Magnetite: The mineral form of iron(II,III) oxide denoted by the chemical formula Fe_3O_4.

*Wüstit*e: The mineral form of iron(II) oxide denoted by the chemical formula FeO.

Newtonian fluid: A fluid that exhibits a proportional relationship between the viscous stresses formed by its flow and the local strain rate.

CHAPTER I

INTRODUCTION

Casting is one of mankind's fundamental manufacturing processes, and it involves the pouring of a molten material into a mold cavity to produce some desired shape. Once the liquid cools and subsequently solidifies within the mold, the part is removed and prepared for its intended application through post-processing. This study focuses primarily on the casting of steel, which was practiced as early as 1200 B.C.E. (McClellan III & Dorn, 2006). As time progressed, several advancements in metallurgical knowledge and technology helped mankind create higher quality steel, namely the Bessemer and open-hearth processes, the electric-arc furnace, and the basic oxygen process.

Although vast technological and scientific advancements have improved the steelmaking process, some steel properties make it considerably difficult to cast even today. Modern casting facilities often utilize casting simulation software to understand and solve these problems associated with steel casting prior to creating the initial prototype. Process simulation software, however, is not perfect. Most packages currently contain highly sophisticated models for common defects such as porosity, but some defects are yet to have a model developed. This leaves the engineer to rely on experience and literature to solve the issues, but in the case of this study, a commercial steel foundry experienced a sporadic, ongoing quality defect that they could not resolve. The company engineers identified that the defect occurs at the mold-metal interface where the liquid steel interacts with bonded chromite sand. The defect, as seen in Figure 1, was described

as a large mass of metal that consumed a portion of the porous section of the mold, and it required strenuous post-processing to remove. The engineers approached the University of Northern Iowa for assistance on resolving the problem.

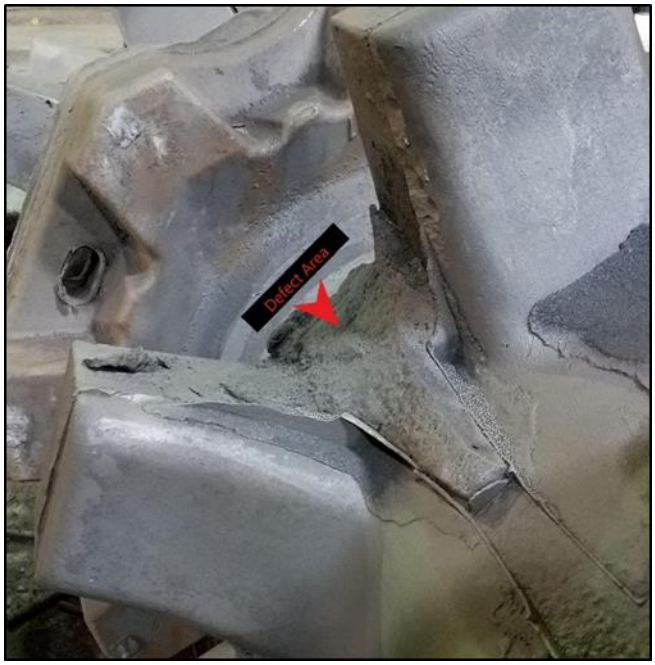

Figure 1: Presentation of the sporadic defect experienced by the commercial foundry. The metal has intruded into the marked section between the two teeth.

Through initial observations, the defect was classified as a metal penetration defect, because metal penetration is defined as the condition where liquid metal intruded into the interstices of the mold. Metal penetration can occur based on several mechanisms which depend on the cast metal. These mechanisms have been thoroughly investigated for specifically steel casting, and it has been concluded that metal penetration of steel could occur by both mechanical and chemical means. Mechanical penetration occurs when the static forces promoting penetration overcome the forces opposing penetration. Diversely, chemical penetration forms through a series of reactions that yield fayalite, a

low melting point iron-silicate. Capillary action then causes metallostatic penetration into the mold as a result of the fayalite reaction. In the case of heavy-section steel casting, the double-skin defect involves both mechanical and chemical mechanisms, which can lead to a case of extreme hybrid penetration.

The objective of this study is to achieve a fundamental understanding of the double-skin defect and the critical conditions for its formation. This understanding will then be used to develop a mathematical model that predicts the formation and propensity of the double-skin defect, which could be manipulated to match the process variables of any production foundry. This tool can then be used by the foundryman to help make informed decisions about what materials and processes should be used to make large steel castings without compromising quality.

Statement of the Problem

What penetration mechanism primarily causes the double-skin defect to form? Can a model be developed to predict the defect to prevent it from happening in the future?

Statement of Purpose

The purpose of this investigation is to understand the conditions of formation of the double-skin penetration defect. Once the conditions are understood and quantified, the information could then be used to create a mathematical model that predicts the defect. This model could then be distributed to commercial facilities to combat the defect in the future, thus providing a preventative tool to the engineers who experience this issue.

Statement of Need and Justification

The current state of process simulation software does not envelop all casting defects that foundries experience. This research would create a mathematical model that will assist the foundry industry's understanding of the causation and prevention of double-skin penetration, thereby decreasing the likelihood of a costly mistake.

Within the industry, the average foundryman age has been recently trending younger. This created a problem, because the retiring generation takes with them years of technical experience that proves invaluable to the emerging generations. The only hope of replacing the experience void left behind by the retirees is to develop and use technology to address problems that were traditionally resolved through experience. This investigation is another step towards that goal.

Hypothesis and Research Questions

What are the favorable conditions for the formation of double-skin penetration?

1. What is the primary penetration mechanism for double-skin formation?
2. Can double-skin penetration be predicted using a mathematical model?
3. What are some possible solutions to prevent double-skin penetration?

Assumptions

The proposed investigation will be completed using laboratory scale equipment, which is assumed to be representative of the industrial scale. All materials provided from the both company and its distributors are assumed to be representative of the commercially available materials.

Limitations

The current state of the model will only be applicable for molds and cores created with chromite sand and bonded by an ester-cured phenolic resin system, as those were the materials related to the specific foundry issue.

CHAPTER II

REVIEW OF LITERATURE

Discussion of Penetration Defects in Metal Casting

Chromite sands have been utilized by many steel foundries for decades, and it has been described as an applicable alternative to silica sand because of its high refractoriness, low thermal expansion coefficient, and high thermal conductivity. While it is true that chromite sand can solve specific issues in steel casting that derive from silica sand, that being veining and finning, it is important to consider that there are defects associated with chromite sand as well. It has been reported that most steel foundries occasionally experience a fused layer of sand on the surface of castings when using chromite materials. This phenomenon, known as metal penetration, was further emphasized in heavy sections and regions of the mold with high thermal saturation (Scott, Thomas, & Strohmayer, 2003).

Metal penetration is defined as the condition in which liquid metal has entered the intergranular space of the molding material, up to and beyond the first layer of sand grains (Draper & Gaindar, 1975). The severity of penetration is classified by both the depth of penetration and whether or not a chemical reaction at the mold-metal interface occurred. Metal penetration can occur based on several mechanisms, but it is generally accepted that mechanical and chemical are the principle mechanisms for metal penetration defects (Stefanescu, Giese, Piwonka, & Lane, 1996).

These phenomena have been thoroughly investigated for both iron and steel casting, and research conducted by the University of Alabama (Stefanescu et al., 1996;

Giese, Stefanescu, Barlow, & Piwonka, 1997; Pattabhi, Lane, & Piwonka, 1996) concluded that cast iron metal penetration defects are always associated with the mechanical penetration mechanism. In the case of steel casting, however, it has been reported that metal penetration can arise from both mechanical and chemical mechanisms, and Table 1 presents the critical factors that influence metal penetration. (Hayes, Barlow, Stefanescu, & Piwonka, 1998; Barlow, Owens, Stefanescu, Lane & Piwonka, 1997).

Table 1: Factors that influence metal penetration defects. (Stefanescu et al., 1996)

Increased penetration	Decreased penetration
Metallostatic pressure	Surface energy
Dynamic pressure	Metal/mold contact angle
Sand grain size	Sand coating
Pouring temperature	Mold density

Metallostatic Pressure

Metallostatic pressure is generated by the sheer weight of the molten metal, which is exerted directly onto the mold interface during pouring and solidification, defined by the equation.

$$P_{st} = \rho g h \quad (1)$$

Where "ρ" is the cast alloy density, "g" is the acceleration due to gravity, and "h" is the height of the metal section above the mold interface. It is known that increasing metallostatic pressure yields a higher propensity for metal penetration, and since the only manipulative variable in the equation is the metal section height, it is more dangerous to create tall casting geometries and risers.

Dynamic Pressure

This condition is only taken into account during pouring, as it occurs when the molten metal enters the casting cavity with turbulence. The dynamic pressure is calculated according to the provided equation.

$$P_{dyn} = \frac{\rho V 2}{2} \quad (2)$$

Where "V" is the instantaneous velocity of the molten metal upon impact with the mold interface. As the dynamic pressure increases, the likelihood of metal penetration relatedly increases. Factors directly impacting the velocity include sprue and pouring height, as well as the cross-sectional area of the gating system, which will directly change the velocity of a liquid according to Bernoulli's principles (Stefanescu et al., 1996).

Sand Grain Size and Mold Density

The average grain diameter of the sand used to create the mold, which is commonly determined per the American Foundry Society's AFS-1105-00-S method, can be used to calculate surface area at the sand interface according to AFS-1109-12-S. Generally, increasing the sand particle size increases the permeability of the sand. Sand permeability can be used to represent the open spaces on the surface of the mold, and an investigation performed by Bryant and Thiel (2017) presented the relationship between the average grain diameter and permeability. From this investigation, it was concluded that as the grain diameter increases, the more open space is available for metal to penetrate, as seen in Figure 2 (Bryant & Thiel, 2017).

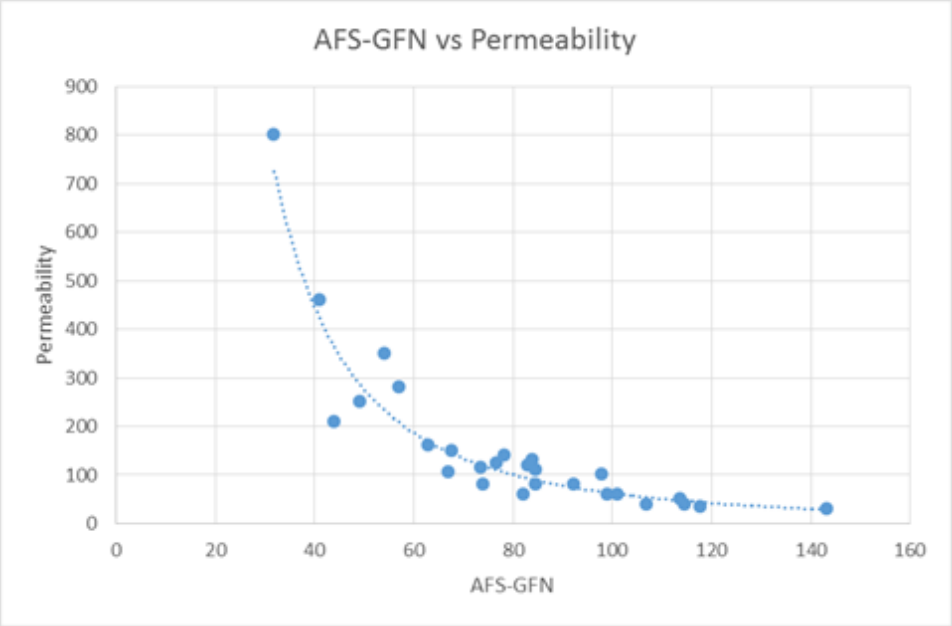

Figure 2: The relationship between AFS-GFN and sand permeability (Bryant & Thiel, 2017)

Surface Energy and Contact Angle

Stefanescu et al. (1996) explained that atoms that are in the same physical state are fundamentally attracted to each other due to molecular force. Within a homogenized mixture of a material of the same physical state, the forces are balanced; however, if two materials of varying physical states are in contact with one another, the atoms will experience different forces because of the difference in state. He concluded that the interfacial atoms are characterized by different energy than the atoms that are only in contact with those of the same physical state. This energy associated with the interfacial atoms is known as surface energy, or surface tension.

In surface chemistry, these variables are measured using the sessile drop methodology, which involves placing a liquid droplet on a solid substrate in open atmosphere, as seen in Figure 3.

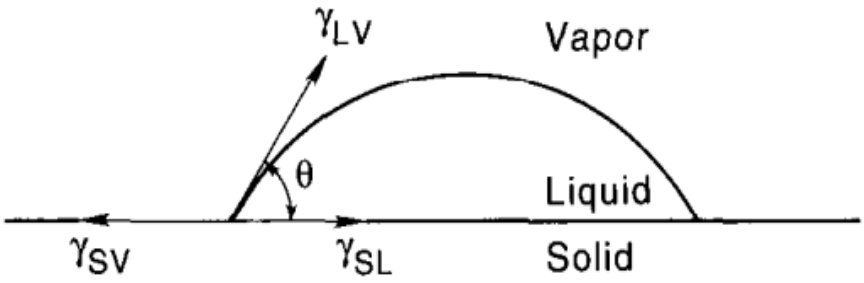

Figure 3: The surface energy balance for a theoretical vapor-liquid-solid system. (Liu & German, 1996)

The shape that the droplet forms is the result of the equilibrium balance of surface energies, which is described by Young's equation.

$$\gamma_{LV}\, cos\, cos\, (\theta) \;=\; \gamma_{SV} - \gamma_{LS} \tag{3}$$

Where "γ_{LV}" is the surface energy associated with the liquid-vapor interface, "γ_{SV}" is the surface energy related to the solid-vapor interface, "γ_{LS}" is the surface energy pertaining to the liquid-solid interface, and "θ" is the contact angle. Since θ and γ_{LV} can be directly measured with relative ease, the capillary pressure can be calculated at the mold-metal interface according the formula.

$$P_\gamma = -\frac{2\gamma_{LV}}{d_e}\, cos(\theta) \tag{4}$$

Where d_e is the average pore size between sand particles. It should be noted that the pressure is highly dependent on the wettability of the material, as if the contact angle is wetting ($\theta<90°$) P_γ will be negative, which indicates that the capillary force will promote penetration. The opposite is also true, because if the contact angle relationship between materials is non-wetting ($\theta>90°$) P_γ will be positive, meaning the capillary pressure will oppose metal penetration into the mold. (Stefanescu et al., 1996)

The contact angle is also directly influenced by the associated temperature. For example, in a different investigation by Stefanescu, the contact angle of liquid iron on silica sand is reported in Figure 4. The relationship indicates that the liquid iron became more wetting as a function of temperature, which, when substituting into the equation for capillary pressure, indicates that high pouring temperature increases the susceptibility of metal penetration by capillary force promotion (Stefanescu, Piwonka, Giese, & Lane, 1993).

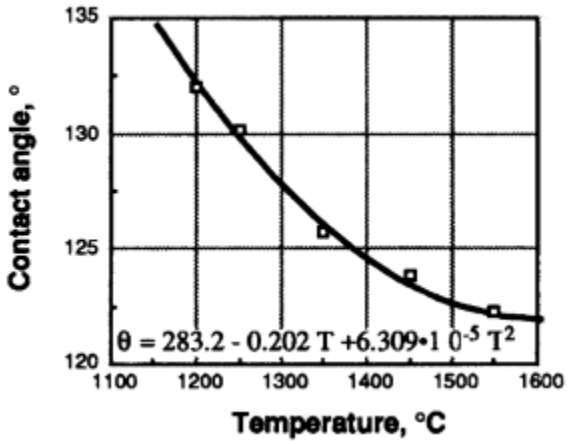

Figure 4: The relationship between contact angle of liquid iron against silica and temperature (Stefanescu et al., 1993).

Friction Pressure

As the liquid metal penetrates into the mold, there will be a frictional resistance factor that retards the metal from penetrating deeper into the interstices. The friction pressure is calculated by the following formula.

$$P_f = \frac{\mu}{K} L_p V_p \quad (5)$$

Where "μ" is the liquid metal viscosity, "K" is the molding sand permeability, "L_p" is the depth of penetration, and "V_p" is the speed of the penetrating metal. Of course, since the sand permeability is directly related to the average sand particle diameter, the frictional pressure changes according to the relationship expressed previously in Figure 2.

Stefanescu's Metal Penetration Model

The aforementioned pressures that are calculated using a variety of process and material variables can then be used in a governing equation that demonstrates the balance of pressure at the mold-metal interface.

$$P_{st} + P_{dyn} + P_{exp} \geq P_{\gamma} + P_f + P_{gas} \quad (6)$$

Where "P_{exp}" is the pressure associated with graphite expansion during solidification, which is irrelevant in steel castings, and "P_{gas}" is the pressure generated by decomposing resin binder, but this value is usually negligible. When the sum of the metallostatic, dynamic, and expansion pressure is greater than the sum of the opposing factors, penetration is predicted to occur.

Review of Fayalite and its Influence on Chemical Penetration

Chemical penetration occurs when there is a mold-metal interface reaction between the molten metal and either the atmosphere or molding media. These reactions allow capillary force to draw molten metal into the interstices of the aggregate (Barlow et al., 1997). The capillary force can oppose gravitational influence and cause penetration defects anywhere on a casting. This mechanism differs from mechanical penetration, since that mechanism generally occurs in the same direction as the gravitational vector. It was first observed by Savage and Taylor (1950) that fayalite was the product of mold-

metal reactions, and they described its mechanism of formation as metal oxidation with a subsequent reaction with quartz. The chemical reaction for fayalite formation is presented (Savage & Taylor, 1950).

$$2FeO + SiO_2 \rightarrow Fe_2SiO_4 \quad (7)$$

An extensive investigation performed by Fisler and Mackwell (1993) realized the kinetics of fayalite formation and growth in a controlled setting. The experiments involved reacting polished single crystal quartz and pre-annealed hematite at 1000-1120℃ (1832-2048°F) under controlled oxygen fugacity conditions at one atmosphere of pressure. The fugacity conditions were selected based on the fayalite stability region defined by O'Neill (1987), as seen in Figure 5. The stability region is represented by the solid lines, which are defined by the quartz-fayalite-iron (QFI) and quartz-fayalite-magnetite (QFM) phase boundaries. The dashed lines represent various forms of iron oxide and iron, including the iron-wüstite (IW), wüstite-magnetite (WM), and magnetite-hematite (MH). The solid circles represent the temperature dependent oxygen fugacity conditions used in their experiments (Fisler & Mackwell, 1993).

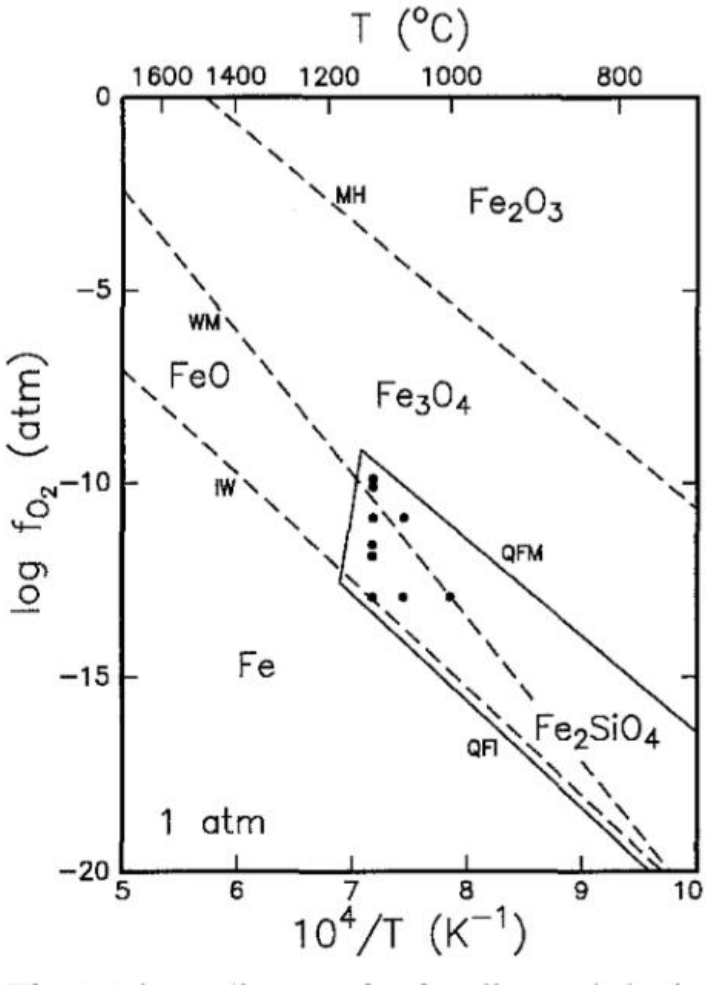

Figure 5: Phase diagram for fayalite and the iron-oxygen system reproduced from Fisler and Mackwell (1993)

Under these conditions, the authors offered three possible diffusion models for fayalite growth that are strictly dependent on one constituent of the reaction being immobile during the diffusion process. Fisler and Mackwell's (1993) models are presented as follows: If the assumption is made that the silicon cannot transport through the fayalite rim, then further development of fayalite occurs by diffusion of iron and oxygen from the wüstite to react at the quartz-fayalite interface. The second coupled

diffusion model is essentially the same as the first, but makes the assumption that the iron is immobile; therefore, the silicon and oxygen from the quartz will diffuse and react with the wüstite-fayalite interface. Lastly, a model that assumed that oxygen immobility suggests counter-diffusion of iron and silicon from the fayalite to react with both interfaces. The authors concluded that the model that assumes silicon immobility had the most support based on a methodology that involved placing platinum markers at the initial quartz-wüstite interface and observing its location after conducting fayalite growth experiments. It was also found that the iron atoms were the most mobile species within the fayalite through a series of diffusivity measurements, and further development of the layer was rate-limited by the grain boundary diffusion of oxygen ions, which further supported the first model. (Fisler & Mackwell, 1993)

Prediction of Chemical Penetration Literature

Barlow et al. (1997) explained that at thermodynamic equilibrium, oxidation of iron initiates when the CO_2/CO ratio exceeds 0.2, which indicated that prediction of chemical penetration tendency in a silica mold could be predicted this way. Casting trials were conducted to investigate this hypothesis. Mold binder type was varied between clay-bonded, sodium silicate, and resin-bonded, and it was found that the CO_2/CO ratio within the mold was constantly changing during solidification and depends heavily on the binder system used to adhere the sand grains. The variability in the CO_2/CO ratio during pouring and solidification drastically changes how chemical penetration occurs in the mold. For example, the critical reactions for a resin-bonded mold are presented in table 2. As seen in the table, several reactions create both carbon monoxide and carbon dioxide for a

resin-bonded mold. This increases the complexity of mathematical prediction, but Barlow measured the CO_2/CO ratio using a mass spectroscopy technique, and a replication of the measurements can be observed in Figure 6. It can be noted that all trials initially exceeded the critical ratio of 0.2, which means one may assume chemical penetration will occur regardless of binder type; however, the defect was only observed on half of the trials.

Table 2: Critical reactions that lead to chemical penetration in a resin-bonded silica mold. (Barlow et. al, 1997)

Reaction	Description
$C + H_2O \rightarrow CO + H_2$	Carbonaceous materials react with water vapor
$C + H_2O \rightarrow CO + H_2$	Dissolved carbon in steel reacts with water vapor
$CO + H_2O \rightarrow CO_2 + H_2$	Formed carbon monoxide reacts with water vapor
$Fe + CO_2 \rightarrow FeO + CO$	Iron oxidized by carbon dioxide at mold-metal interface
$C + ½O_2 \rightarrow CO$	Atmospheric oxygen reacts with dissolved carbon in steel

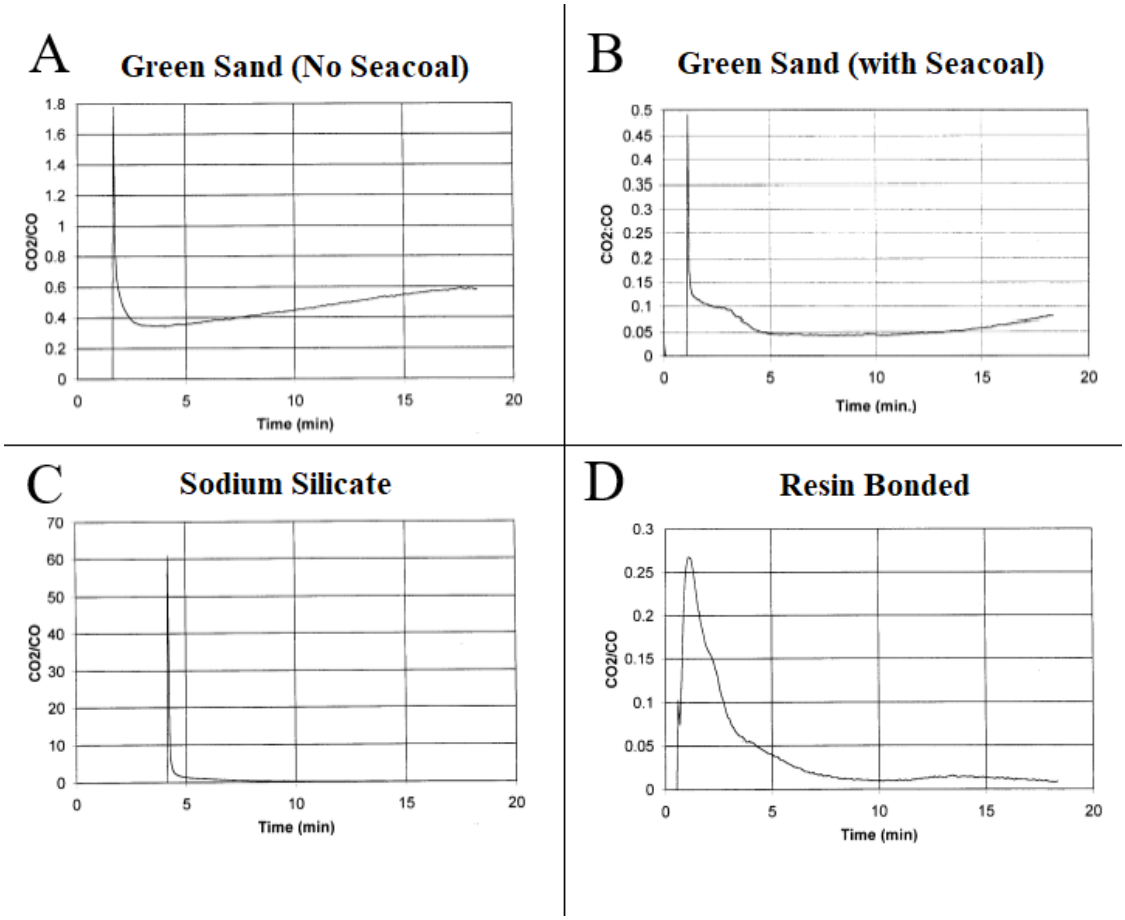

Figure 6: Replication of CO_2/CO ratio measurement results (Barlow et. al, 1997).

Barlow et al. (1997) then proposed a model based on the prediction of a decarburized surface of the casting through carbon diffusion. An equation was given to calculate the critical carbon content, C_{cr}, of the steel as seen in the presented equation.

$$C_{cr} = \frac{p_{CO_2}^3}{p_{CO}^2}[0.1 * exp\ exp\ (0.002T)\ ] \quad (8)$$

Where p_{CO} and p_{CO2} are the partial pressures associated with carbon monoxide and dioxide respectively, and T is the temperature of the cast steel. A one-dimensional finite difference model was then created to calculate carbon diffusion through the solidifying

layer of steel according to the fraction solid. This model yielded the interfacial carbon content, which was then compared to the critical content, which are both temperature dependent. Barlow et al. (1997) explained that when the critical carbon content exceeds the interfacial carbon content during solidification, iron oxide will form on the surface, and this was how chemical penetration was predicted. The results predicted chemical penetration more successfully than the initial model based on the CO_2/CO ratio, but it was concluded that improvements could be made when prediction technology advanced further.

It can be concluded from prior research that the risk of chemical penetration increases when there is ample wüstite to react with quartz, which heavily depends on oxygen potential in the mold atmosphere and carbon absence at the metal interface. If the formation of iron oxide is suppressed a required step for fayalite formation at the mold-metal interface is unattainable. Theoretically, this means no chemical penetration would occur. It is known that a reducing atmosphere in the mold can eliminate formation of iron oxide from the metal, which is supported by Barlow et al.'s (1997) investigation; however, in the case of chromite sand, iron oxide in the form of wüstite is provided from the aggregate itself, which appears to accelerate the process of chemical penetration.

The Unique Properties and Characteristics of Chromite Sand

The chemical composition for the mineral "chromite" is $FeO \cdot Cr_2O_3$; however, Scott et al. (2003) claims that what is often referred to as chromite sand is not purely chromite, but rather a blend of minerals that relate to the spinel archetype (Scott et al., 2003). A general depiction of chromite sand is brilliantly described by Gillson (1971) as:

$$(Mg, Fe +2)O \cdot (Cr, Al, Fe +3)_2O_3 \text{ (Gillson, 1971)} \quad (9)$$

Chromite sand is further complicated since quantities of each compound vary depending on which deposit it was collected from. Table 3 shows the reported ranges of some of the large chromite sand distributors from McBane's (personal communication with Scott, 1971) personal report data (Scott et al., 2003).

Table 3: Ranges of chromite sand chemical composition from various distributors (Scott et al., 2003).

Mineral	Molecular Formula	Reported Range of Weight Percentage
Chromia	Cr_2O_3	44.8 – 64.1
Wüstite	FeO	12.2 – 27.0
Quartz	SiO_2	1.0 – 7.3
Magnesia	MgO	8.4 – 19.1
Lime	CaO	trace – 1.0

As seen in the table, when chromite is mined it can be found with siliceous materials that are detrimental to its refractoriness. (Scott et al., 2003) These contaminants are thought to cause the mold-metal interface reactions that lead to chemical penetration in chromite molds and cores. To counteract this for foundry grade molding materials, a Steel Castings Research and Trade Association (SCRATA) specification defined the maximum quartz and lime content in foundry grade chromite sand as 4% and 0.5% respectively (Middleton, 1973). The Steel Founders Society of America (SFSA) presently defines the maximum quartz content as less than 3% (SFSA, 1967). To reduce the level of contamination, chromite can be separated from gangue because of its density, for example with a spiral separator, or its unique magnetic properties (Scott, 1993).

It has been identified that naturally occurring clays should be considered as detrimental contaminants in chromite sand as well, which lead to the development of a process to wash the sand before it's permitted for foundry applications. In the past, the initial washing performed in Africa proved insufficient for removing the gangue. This lead to the standard practice of mineral importers washing the sand a second time, which created the "double washed" designation (Scott et al., 2003). According to a consultant, the process of rewashing the sand was recently eliminated in the United States because of environmental concerns. In response, chromite rewashing was relocated to Africa, where the quality of water used could be questioned since environmental requirements aren't as stringent (Luth, 2010).

Even when chromite sand is properly prepared for foundry applications, the elevated temperatures the aggregate experiences during casting causes a variety of phenomena to occur. It has been reported that under a reducing atmosphere the iron present in chromite can migrate to the surface of the grain when heated. This natural phenomenon was described as a diffusion with subsequent oxidation taking place above 600°C, and is supported by indirect observations of chromite sand "rusting" after use. Scheffer (1975) expressed a concern that the iron coating could reduce the sand surface energy and subsequent reuse of the material would cause the liquid steel to wet the coated grains, which could be why few foundrymen consider chromite sand reclamation processes feasible. In the case of an oxidizing atmosphere both the chromium and iron cations are reported to convert to the positive valence state of R_2O_3. This series of reactions yields a ceramic bond which is responsible for the increased hot strength

exhibited by chromite molds and cores, and also accounts for the weight gain typically observed when chromite sand is subjected to a loss on ignition test (Scheffer, 1975).

Review of the Double-Skin Defect

Scott et al. (2003) also explains that at even higher temperatures, for example at the mold-metal interface of steel castings, the iron oxides present in the chromite sand can react with gangue or clays and form fused masses. These reactions can cause a case of extreme penetration, known by the foundry industry as the double-skin defect (Scott et al., 2003). There was a recent study conducted by Ravi, Thiel, Bryant, Giese, and Schneiter (2018) that investigated the high temperature characteristics of chromite sand with different levels of silica contamination in an attempt to understand the cause of the double-skin defect. This work involved using an aggregate dilatometer to measure the sample deformation, surface viscosity, and sinter temperature of several chromite samples doped with silica sand. The linear expansion results from Ravi et al.'s (2018) investigation are presented in Figure 7. Interestingly, the silica caused an expansion of the sample around 450℃, which could be attributed to the phase transition of quartz at elevated temperatures. More importantly, it can be observed from the figure that increasing silica content caused a rapid contraction of the sample to occur at progressively lower temperatures.

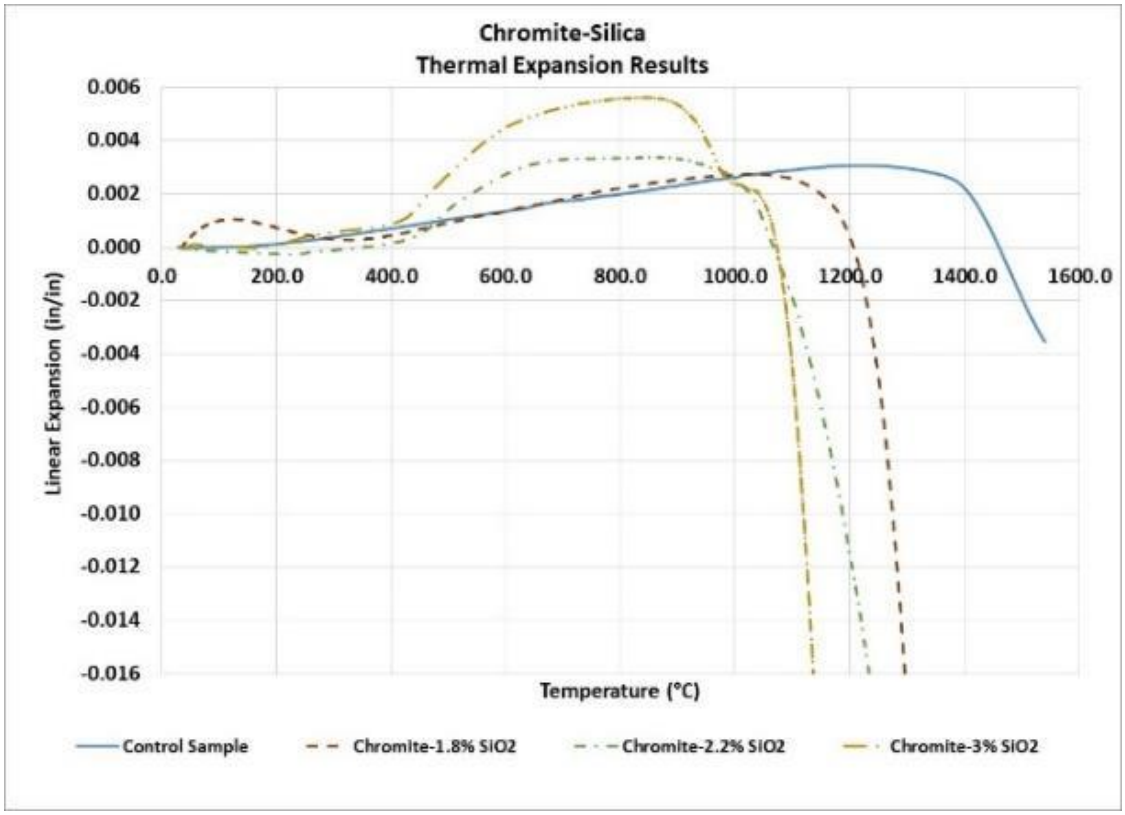

Figure 7: Thermal expansion results from chromite sand doped with various quantities of quartz (Ravi et al., 2018).

Fayalite has a significantly lower liquidus temperature than its constituents, as seen by the wüstite-quartz phase diagram in Figure 8 (Luo, Zhu, Zhou, & Zhang, 2015). It can be inferred from Ravi et al.'s (2018) investigation that fayalite formation in the samples doped with silica sand caused the fusion temperature of the sand to drastically decrease. In Ravi et al.'s (2018) investigation, the sinter temperature results obtained from the aggregate dilatometer were compared to a simulated temperature profile of a chromite core used in a large, commercial steel casting that variably experienced double-skin penetration. The mold was simulated to stay at temperatures above the calculated

sinter temperature of the sand for approximately 4 hours. If the conditions for fayalite formation are favorable in this case, then the sand would theoretically have 4 hours to react, melt, and draw liquid metal into the interstices of the mold. It was then concluded that while the maximum silica content of chromite sand was specified by the industry as 3.0%, section thickness of the casting and the associated temperature has a critical role (Ravi et al., 2018).

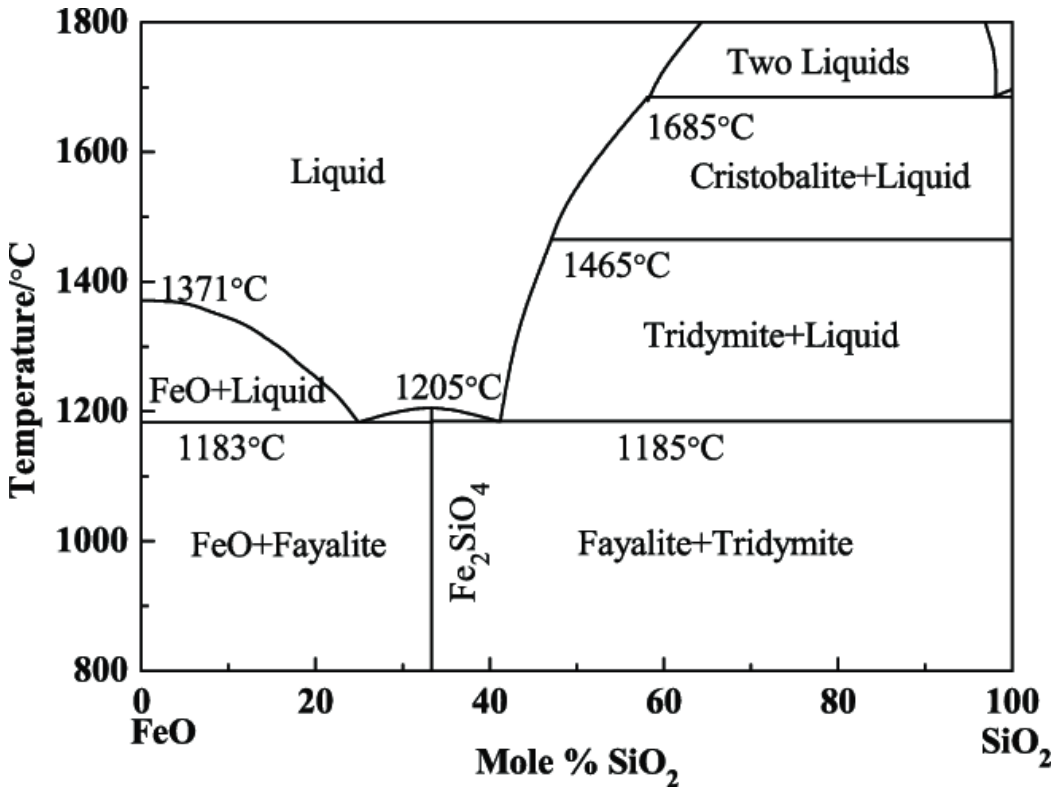

Figure 8: The wüstite-quartz phase diagram, which illustrates the decrease in liquidus temperature associated with fayalite at the eutectic point (Luo et al., 2015).

Liquid Fayalite's Theoretical Behavior within the Mold

In a polydispersed grain assembly, the physics behind liquid behavior in a medium become quite complex, but Shaw explains that the fundamentals of a two-pore size model can illustrate important features of liquid behavior, which is critical to the understanding of what phenomena can be expected to occur in a medium with various grain sizes (Shaw, 1986). Once a liquid is introduced to a dry, porous medium, it isolates itself at the grain contacts until some critical pressure (Bredt, 1995) or liquid fraction is reached, as seen in Figure 9 (A). Once one of these conditions are reached, pores with the smallest coordination number begin to fill with liquid, exhibited by Figure 9 (B). Upon total saturation, progressively larger pores will fill if sufficient liquid is available (Shaw, 1986). This eventually creates a fluid network in the medium that consists of the smallest pores that form a continuous trail throughout the interstices (Bredt, 1995).

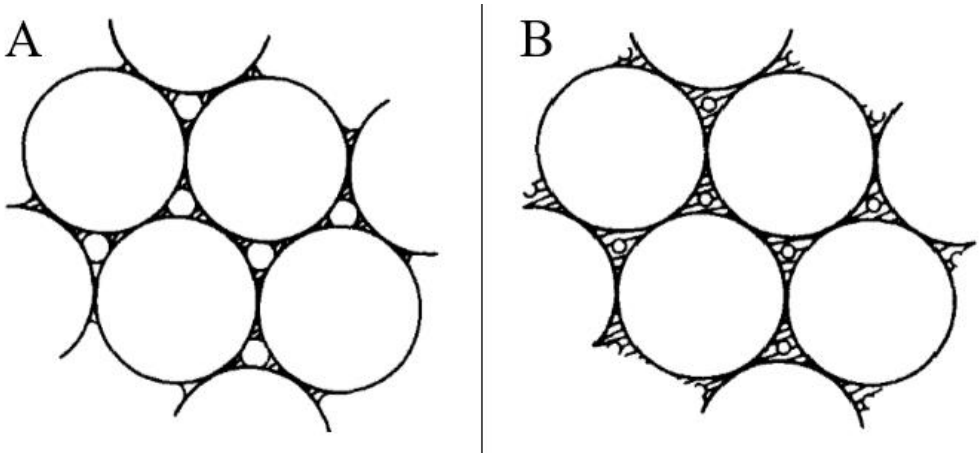

Figure 9: Illustration of liquid behavior in a porous medium, where "A" exhibits liquid isolation (the shaded regions) at the grain contacts, and "B" shows how the pores progressively fill with increasing liquid fraction (Reproduced from Shaw, 1986).

To relate these concepts to the double-skin defect in steel casting, conditions for fayalite formation must be favorable. The following conditions are hypothesized to be the critical contributors to this reaction based upon previous research. Firstly, the temperature dependent oxygen fugacity should be within the fayalite stability region, and the activation energy for fayalite formation must be reached. Fayalite can then form at the wüstite-quartz interfaces present in a chromite mold according to the aforementioned immobile-silicon diffusion model. Since liquid fayalite is a wetting liquid with a contact angle between 10-30° depending on the substrate (Fukuyama, Donald, & Toguri, 1997), a network could then form in the mold at these interfaces if it surpasses the sinter temperature. If there is contact between the fayalite network and the liquid steel, capillary force will cause what Lenormand (1989) describes as invasion percolation, which was originally theorized by Wilkinson and Willemsen (1983). The liquid steel reservoir, which has essentially infinite volume in this case because of risering, feeds metal into the interstices through the liquid fayalite network until some critical solid fraction renders the solidifying steel immobile.

CHAPTER III

EXPERIMENTAL METHODOLOGY

Test Mold Preparation

A test casting was developed to measure the temperature dependent CO/CO_2 ratio within a mold. The design is based on the test mold utilized in Barlow's investigation (Barlow et al., 1997), and it can be observed in Figure 10. The hidden, or dashed lines represent the dimensions of the core geometry.

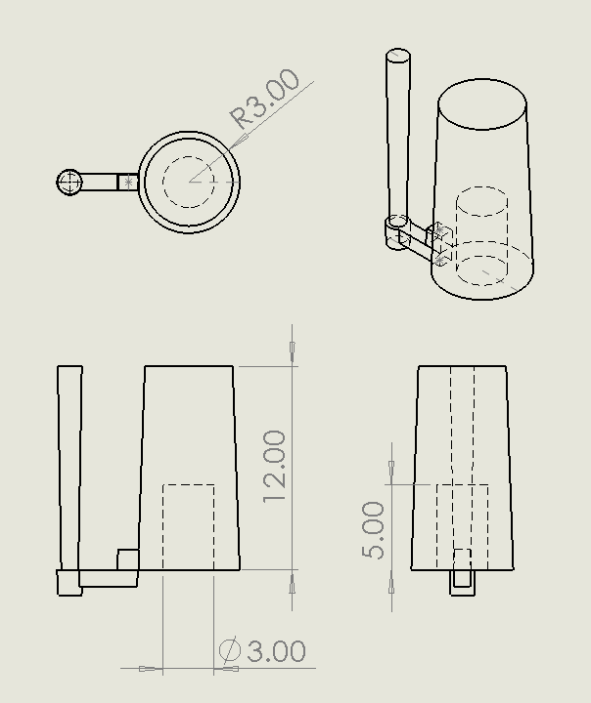

Figure 10: Schematic illustration of the test casting design. The cavity dimensions are representative of the core. All dimensions provided are in inches (Barlow et al., 1997).

50lb (22.68kg) of a commercially available three screen, 57 GFN silica sand was placed in a vibratory mixer. A commercial ester-cured phenolic resin system was used to prepare the molds. Three different resin contents were used, which were 1, 1.25, and

1.5% based on sand weight. This mixture was placed in the test mold pattern. The resultant test molds, upon stripping from the pattern, were allowed to remain idle for 24 hours before further testing was conducted.

Chromite Core Preparation

The 3” x 5” cylindrical test cores required for testing were prepared using the same ester-cured phenolic resin system as the molds. Instead of silica sand, the cores were created using a commercially available high-purity chromite sand that is specified to have a quartz content of less than 0.5%. The sand was initially split using a 16-way sand splitter to ensure a representative sample of the bulk material. 3000g (6.614lb) of split material was then placed in a desktop mixer, where ester-cured phenolic co-reactant was introduced at 30% based on calculated resin weight. After mixing for 60 seconds, the mixture was flipped to ensure homogenization. Three different resin contents, which matched those used in mold preparation at 1, 1.25, and 1.5%, were used. The appropriate quantity of resin was then added, and the same mixing methodology was repeated. The final mixture was placed in a sample core pattern, where the cores were allowed to cure until they reached strip time. The resultant cores were placed in a desiccator for 24 hours before further testing.

Determination of Core Atmosphere CO/CO_2 Ratio during Pouring and Solidification

An 8mm (0.315in) stainless steel sample extension tube was placed within the test core of the assembled mold, 0.5in (12.7mm) from the mold-metal interface (see Figure 11). The molds were cast with WCB steel at 2900°F (1593°C), and gases produced during casting were drawn into the sampling line at a rate of 1 liter per minute and analyzed for

CO, CO_2, and O_2 content using a Testo 350 portable flue gas analyzer. A polyethylene filter was used in the sampling line to eliminate moisture and particulate matter in the system. The extension tube was also mounted with a type-K thermocouple that was placed 0.5in (12.7mm) from the mold-metal interface. This thermocouple was connected to a data acquisition unit to additionally create temperature dependent results.

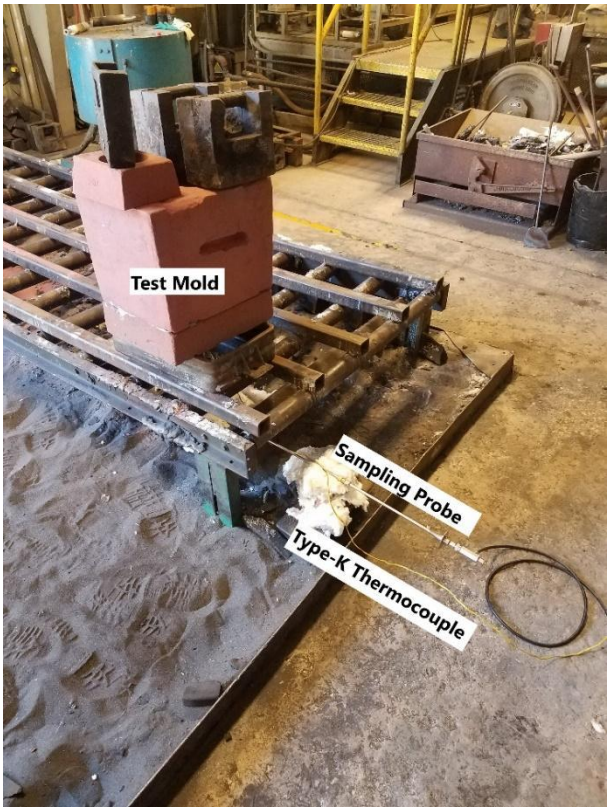

Figure 11: Testing arrangement for collection of CO/CO_2 emissions during casting.

The oxygen fugacity was then calculated using the CO_2/CO ratio results according to the following formula (Fegley, 2012):

$$f_{O_2} = \left[\frac{X_{CO_2}}{X_{CO}}\right]_{eq}^{2} \times \left(\frac{1}{K_p}\right)^{2} \quad (10)$$

Where

- f_{0_2} is the oxygen fugacity
- X_{CO_2} is the carbon dioxide content
- X_{CO} is the carbon monoxide content
- K_p is the equilibrium constant given by $K_p = e^{-\Delta G°/RT}$
    - ΔG° is the Gibb's free energy associated with the fayalite reaction
        - ΔG° = -39,140 + 15.59T J/mol (Jacob, Kale, & Iyengar, 1989)
    - R is the gas constant (8.31441 J/K·mol)
    - T is the temperature in Kelvin
    - e is the mathematical constant known as the base of a natural logarithm

Determination of Specific Heat Capacity for High-Purity Chromite Sand

Using a differential scanning calorimeter, the specific heat capacity of bonded chromite samples with 0.17% silica contamination was determined using an IsoStep DSC temperature program. The IsoStep DSC program is advantageous as it is the preferred method for determining the specific heat of a sample during chemical reactions and physical transitions. In this program, the temperature dynamically increases at a rate of 15°C (27°F) per minute until a specific target temperature for an isothermal hold is achieved. The aforementioned isothermal holds were installed every 200 degrees from room temperature to allow the sample to reach thermal equilibrium in the furnace before progressing to the next temperature ramp. This methodology for specific heat determination required 3 tests for each sample. Firstly, the described temperature program was conducted on a blank sample, which consisted of a reference alumina

crucible without a lid. Following the blank, a calibration sample was tested. During this trial, one of the crucibles was equipped with a lid, and the difference in mass was compared to the crucible used in the blank trial. Lastly, a 20 ug sample of the bonded chromite was placed in the crucible used in the calibration process and sealed with a lid. The evaluation routine then determines the amplitude of each sample using Fourier analysis, and the specific heat capacity as a function of temperature was determined using the following formula (Toledo, 2002).

$$c_p = \frac{(A_s - A_{Al}) * m_{Al}}{m * (A_{Al} - A_b)} \, c_{p_{Al}} \tag{11}$$

Where

- C_{pAl} is the specific heat capacity of the alumina
- A_s is the amplitude associated with the sample
- A_{Al} is the amplitude associated with the alumina
- A_b is the amplitude associated with the blank
- m_{Al} is the mass of the alumina
- m is the mass of the sample

Determination of Sinter Temperature of Chromite Sand with Different Concentrations of Silica Contamination

A methodology proposed by the University of Northern Iowa (Thiel & Ravi, 2014) built upon research presented by Tardos, Mazzone, and Pfeffer (1984) to measure the surface softening of a granular substance at elevated temperatures. Thiel explains that the surface viscosity measurement is based on the compaction of the sand particles while

under a compressive load and constant heating rate. Sand particles are porous in nature, and will initially expand with increasing temperature, but subsequently contract due to sintering, which occurs at the intergranular contact points. This phenomena is a result of surface softening and deformation at the concentration point of the compressive load. These soft particles were assumed to behave as a Newtonian fluid, based upon which, Thiel and Ravi (2014) claims the surface viscosity can be defined (Thiel & Ravi, 2014).

Using a similar methodology to Ravi et al.'s (2018) the high temperature characteristics of chromite samples doped with silica sand were determined using a high temperature aggregate dilatometer. The cylindrical sample geometry was identical, with an approximate height of 1.6in (4.06cm) and a 1.1in diameter (2.8cm). These samples were prepared using a commercial ester-cured phenolic resin system at an addition rate of 1.5% based on sand weight. The sample deformation was recorded at a heating rate of 2℃ (3.6°F) per minute, and these results were used to calculate the surface viscosity and associated sinter temperature.

Calculation of Surface Viscosity and the Associated Sintering Temperature

The deformation recorded from the dilatometer was used to calculate the viscosity of the bonded samples. The following formula was used to calculate the viscosity (Thiel & Ravi, 2014):

$$\eta_s = KF_pD_p^{-2} / [\partial (f\Delta l/2l_o)^{0.5} / \partial t^n]^{1/n} \quad (12)$$

The coefficient ‘n’ is the slope of Δl vs. time on a log plot. The coefficient ‘n’ was determined to take a value of 0.47-0.5 in each experiment. Assuming ‘n’ to be 0.5, the formula reduces to (Thiel & Ravi, 2014):

$$\eta_s = KF_pD_p^{-2} / [\partial (f\Delta l/2l_o) / \partial t] \quad (13)$$

Where

- The denominator is the slope of the deformation versus time.
- The constant $K = 2/5\pi$,
- D_p is the particle diameter,
- F_p is the inter-particle compression force given by: $F_p = 4\varepsilon D_p^2 L/\pi (1-\varepsilon) D_s^2$
    - ε is the porosity of the sample
    - L is the load on the sample
    - D_s is the diameter of the sample holder
- $\Delta l/l_o$ is the linear expansion/contraction measured from the dilatometer.
- The coefficient f is given by $3\beta/2$
    - β is the layer spacing and is given by

$\beta = \sqrt{(2/3)} * \{\pi/[3\sqrt{2} (1-\varepsilon)]\}^{1/3}$

Additionally, the quartz content of the samples was realized using a XRF spectrometer. This methodology involved pulverizing the specimen into a fine powder using a mortar and pestle. The resultant powder was inserted into the spectrometer sample holder, where three point calibration curves were used for quartz content determination.

CHAPTER IV

RESULTS AND DISCUSSION

Results of Core Atmosphere CO/CO_2 Ratio Measurements during Pouring and Solidification

The data collected from the first sample, which contained 1% ester-cured phenolic resin, is presented in Figure 12. After pouring, a sharp increase in both carbon monoxide and dioxide was observed, and both contents peaked roughly 200 seconds after pouring began. Carbon monoxide content was significantly higher than carbon dioxide, reaching a maximum amplitude of approximately 140ppm, while carbon dioxide content barely surpassed 40 ppm. Carbon monoxide and dioxide concentration stabilized after 1600 and 1000 seconds respectively.

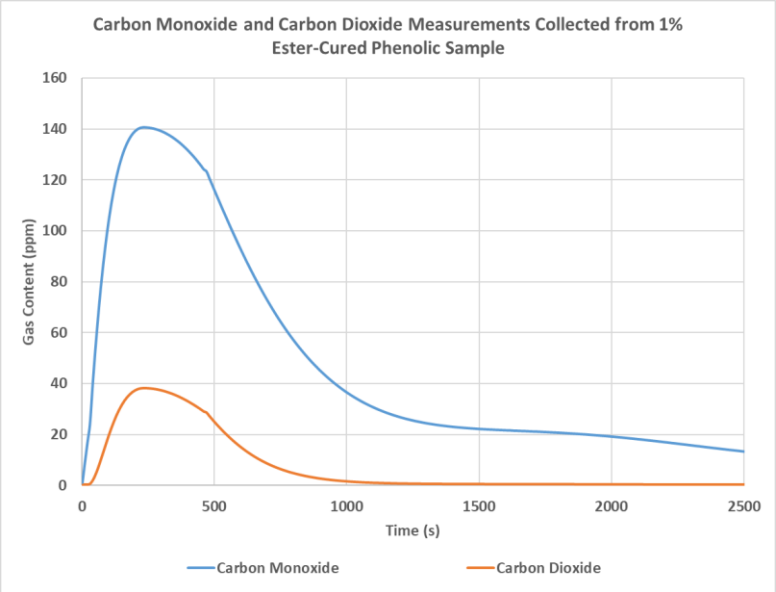

Figure 12. CO and CO_2 concentrations measured from the 1% ester-cured phenolic chromite sample.

Using the concentration data from the 1% ester-cured phenolic sample, the CO_2/CO ratio was calculated as a function of time as seen in Figure 13. As expected, there was a significant increase in the ratio just after pouring, with the maximum amplitude being reached at approximately 250 seconds. The ratio stabilized after roughly 1300 seconds, which is close to the median stabilization time observed in the concentration data between carbon monoxide and carbon dioxide. When comparing this result to those presented by Barlow et al. (1997), this measurement was most similar to the resin-bonded sample provided in Figure 6 (D). Interestingly, the ratio surpassed 0.2, indicating that the oxidation of iron could've occurred at the metal-interface in this trial.

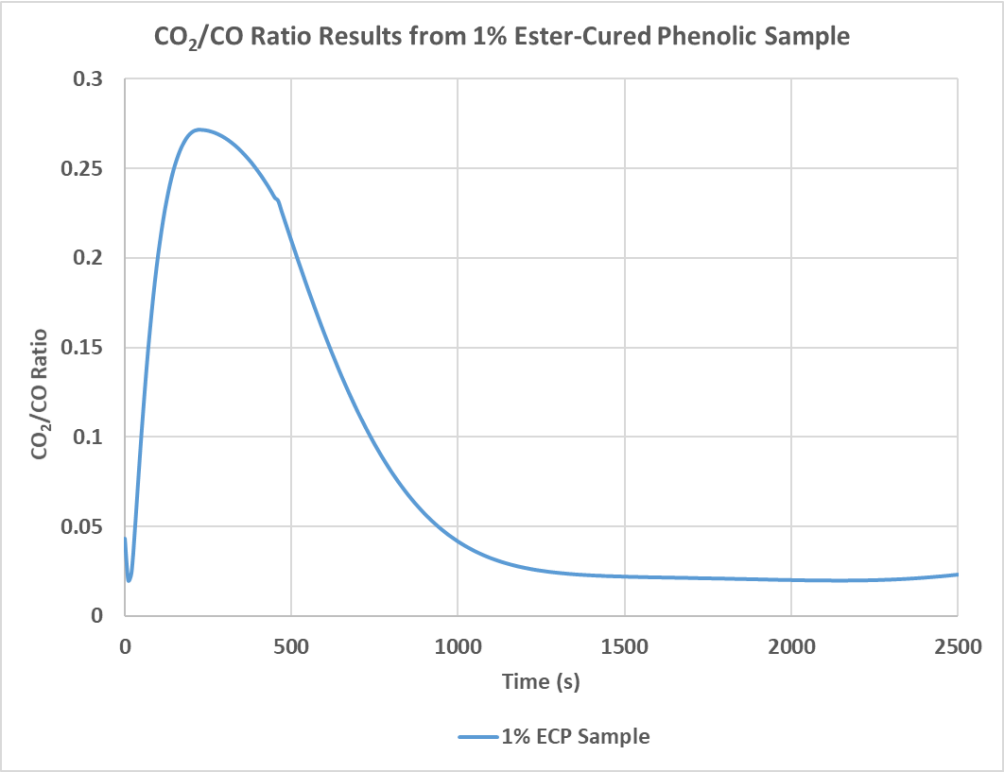

Figure 13. CO_2/CO ratio calculated from the concentration data measured from the 1% ester-cured phenolic sample.

A similar trend can be observed by the 1.25% ester-cured phenolic sample in Figure 14. In this trial, the overall amplitude of the carbon monoxide and carbon dioxide curves increased slightly, with a value of approximately 180 and 60 ppm respectively. The peak value was maintained for a longer period of time for this sample, around 200 seconds. 300 seconds after pouring, both gasses decreased in concentration until they stabilized at approximately 1500 seconds.

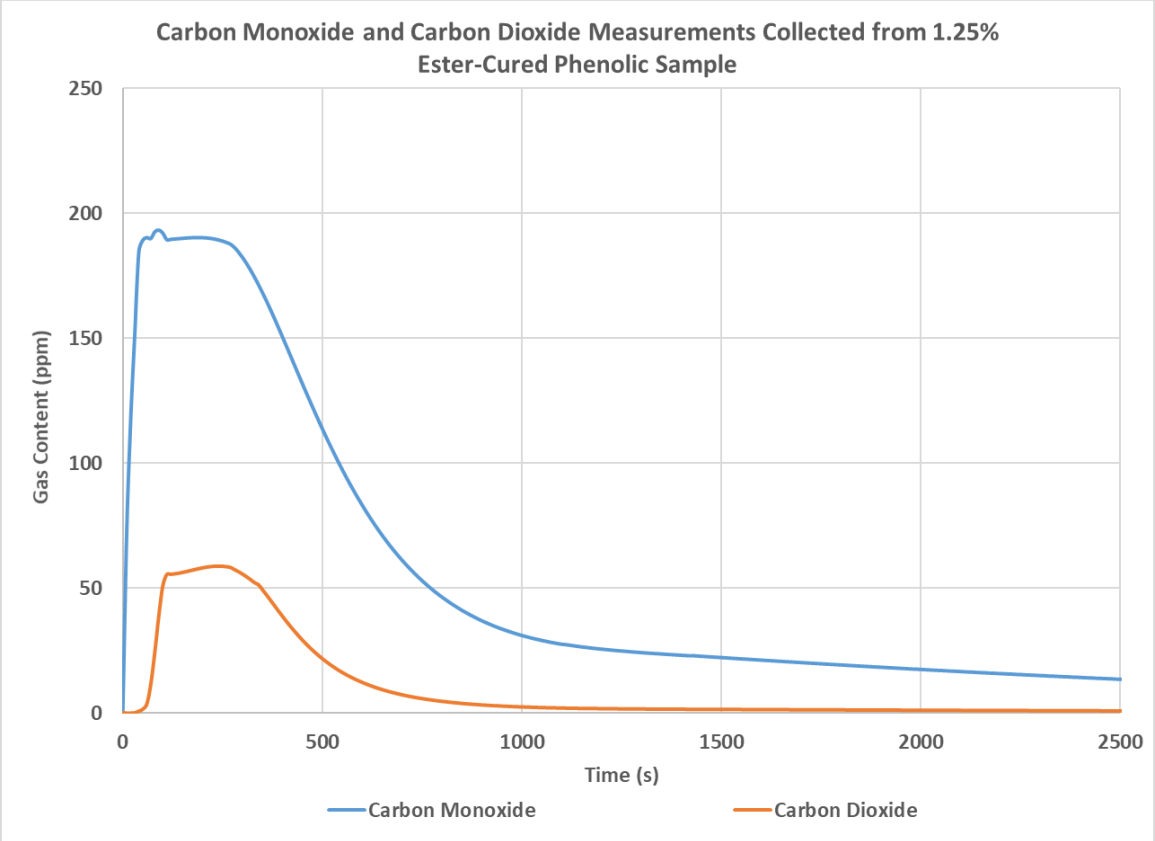

Figure 14: CO and CO_2 concentrations measured from the 1.25% ester-cured phenolic chromite sample.

The CO_2/CO ratio results were quite similar, as seen in Figure 15, but the peak value was slightly higher in this sample at 0.32. This result was likely due to slight

variability in pouring temperature, as the sand sample in this trial surpassed the maximum temperature reached by the 1% trial. In this case, the ratio stabilized at a slightly higher ratio than the prior sample, with a value of .07 compared to .03. However, the two samples did stabilize at similar times after pouring began.

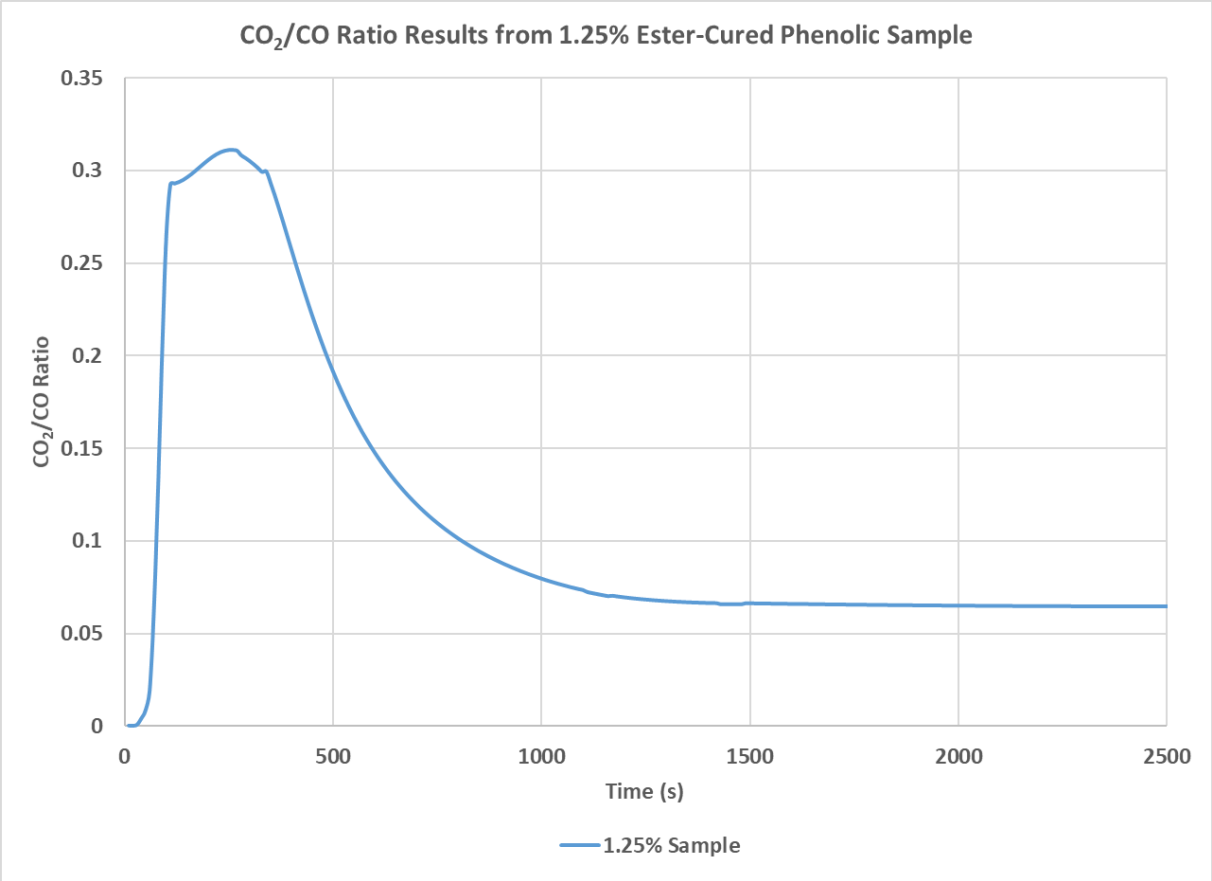

Figure 15: CO_2/CO ratio calculated from the concentration data measured from the 1.25% ester-cured phenolic sample.

The gas concentration data for the final trial, which contained 1.5% ester-cured phenolic resin, is provided in Figure 16. As seen within the figure, there was a slight change in peak amplitudes compared to the other samples. The carbon monoxide content reached a peak value of 160ppm approximately 180 seconds after pouring began, and

carbon dioxide showed a similar trend with a peak value of 45 ppm. Interestingly, the 1.25% sample exhibited higher amplitudes than the 1.5%, which was not an expected result.

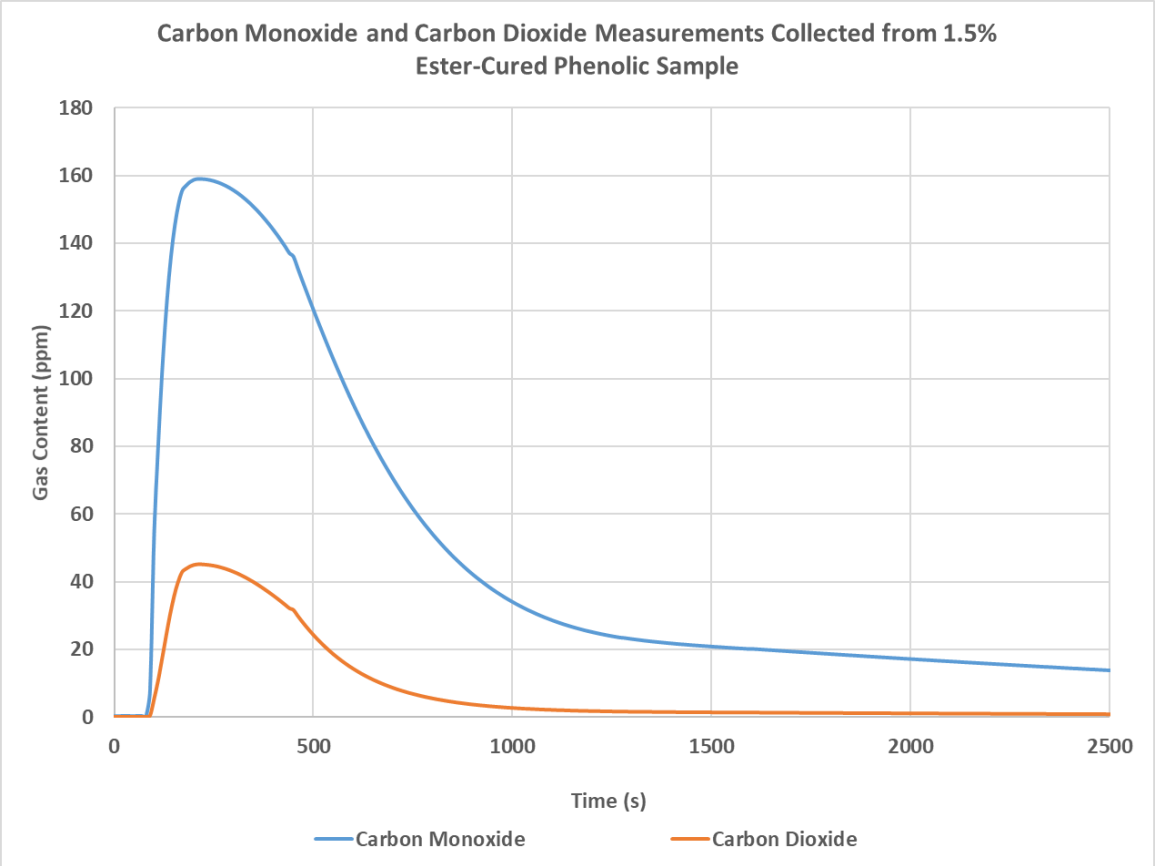

Figure 16: CO and CO_2 concentrations measured from the 1.5% ester-cured phenolic chromite sample.

Lastly, the CO_2/CO ratio was calculated for the final, 1.5% ester-cured phenolic sample, and the data may be observed in Figure 17. The peak amplitude of the ratio was 0.28, which was a value between the two previous, similarly to the concentration data of

this sample. Upon reaching the stabilization ratio at 1200 seconds, this trial exhibited a similar trend to the 1.25% sample with a value of 0.07.

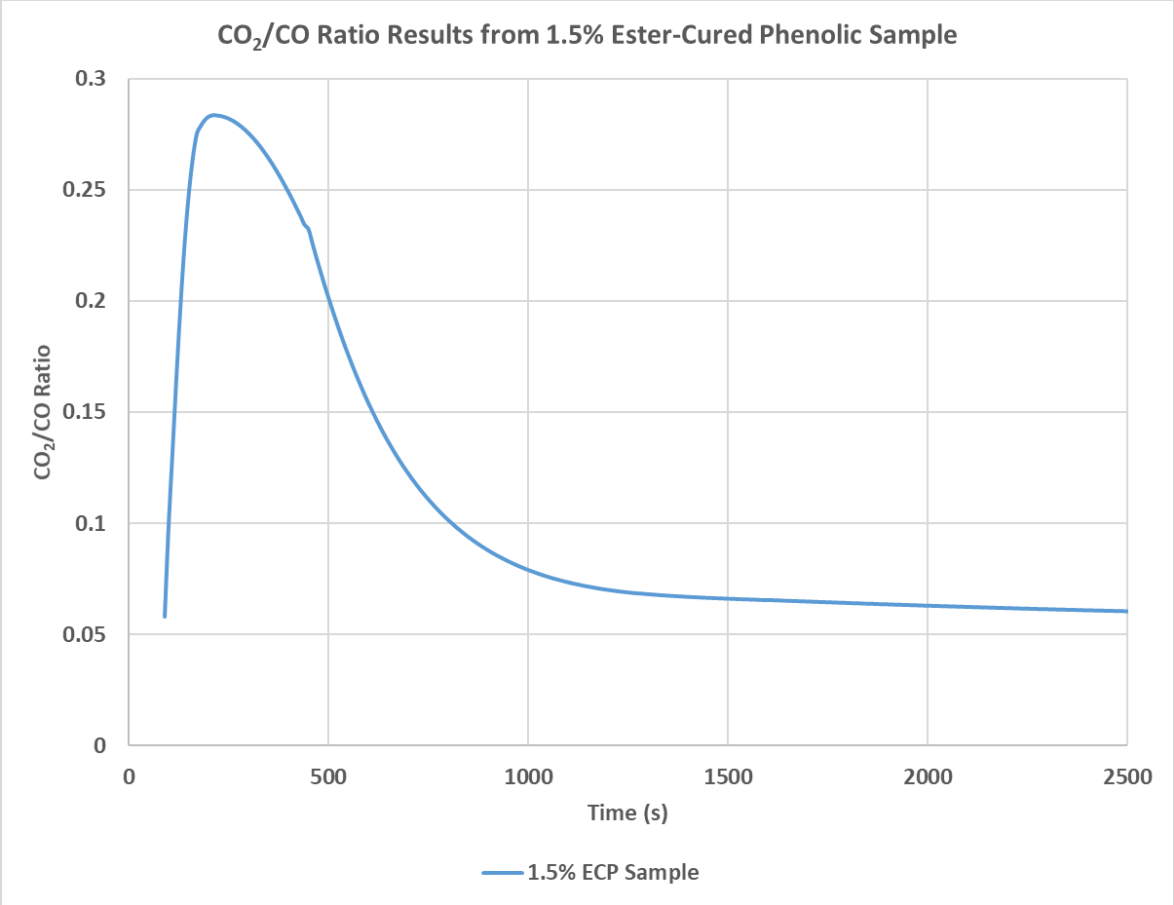

Figure 17: CO_2/CO ratio calculated from the concentration data measured from the 1.5% ester-cured phenolic sample.

The CO_2/CO ratio results were then used to calculate the temperature dependent oxygen fugacity as described within the experimental methodology. The resultant fugacity values were then plotted as a logarithmic function with respect to temperature, as seen in Figure 18. As seen within the figure, the data was coupled with the fayalite stability region in a similar manner as Fisler and Mackwell's (1993) investigation. The

dashed lines represent an extrapolated calculation of the QFI and QFM phase boundary. It can be observed within the figure that, despite increases in total binder content, the oxygen fugacity remained constant between samples. Using a logarithmic regression curve on each of the three datasets, the intersection point between each of the fugacity series and the extrapolated QFM phase boundary was realized mathematically. It was found that the average intersection point between the three samples was 1434°C (2613.3°F).

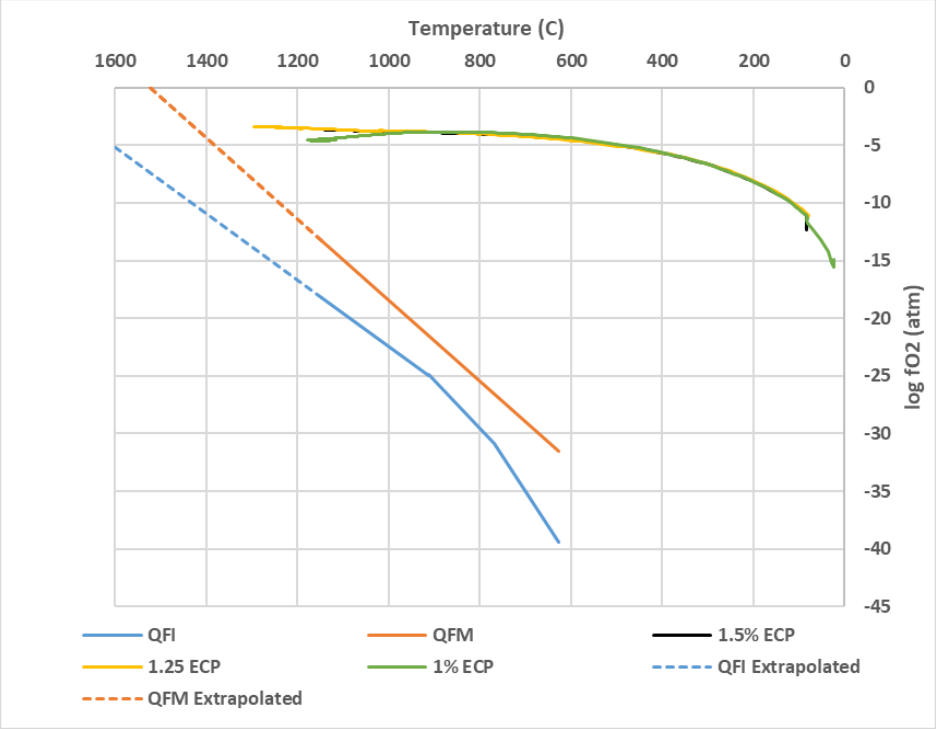

Figure 18: The relationship between the logarithmic oxygen fugacity and sand temperature with relation to the fayalite stability field defined by O'Neill (1987)

Differential Scanning Calorimetry Specific Heat Capacity Results

The specific heat capacity results for the high-purity chromite sample are shown in Figure 19. It can be observed that the specific heat capacity of the sample was approximately 650 J/kg·°C (157.9 btu/lb·°F) at room temperature. The specific heat capacity steadily increases with relation to temperature up to 925°C (1697°F), where the sample reached a peak value of 1526 J/kg·°C (364.47 btu/lb·°F). After the peak, the sample result was observed to decrease until the conclusion of the trial at 1600°C (2912°F).

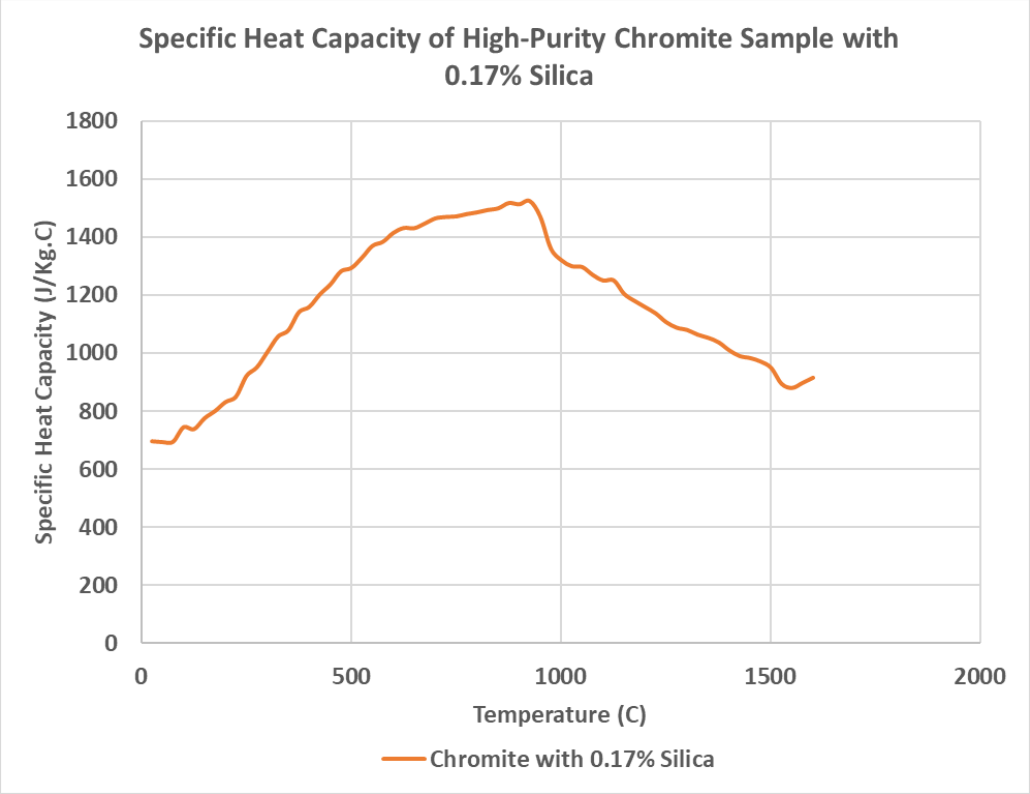

Figure 19: Specific heat capacity results presented as a function of temperature for the high-purity chromite sample.

Dilatometry Results for Linear Expansion, Surface Viscosity, and Sinter Temperature

The quartz content of each sample, determined through XRF spectroscopy, is supplied in Table 4. The baseline sample was the same material as used in the specific heat capacity trial, with a low quartz content of 0.17%. The next samples were purposely contaminated with excess quartz, and the concentration was determined to be 0.84%, 1.78%, and 2.56%. These samples represent most of the quartz content specification range supplied by the industry, defined as ≤ 3%.

Table 4: Quartz concentration results of linear expansion samples obtained through XRF.

Quartz Concentration Results from XRF				
Sample #	1	2	3	4
%SiO_2	0.17	0.84	1.78	2.56

Linear Expansion Results

Similarly to results reported by Ravi et al. (2018), the linear expansion results of the bonded chromite sand samples are supplied as a function of temperature in Figure 20. All samples displayed similar expansion profiles for the first 400°F (204°C). Once the samples surpassed that threshold, the behavior became more unique. The high-purity, 0.17% sample showed the highest thermal stability, reaching peak expansion at approximately 2200°F (1204°C) before rapidly contracting at 2550°F (1339°C). The 0.84% and 1.78% samples behaved similarly until 1000°F (538°C), but the 0.84% sample continued to expand at a higher rate until 2100°F (1149°C) where it reached a peak value that doubled the high-purity sample amplitude. The increase in quartz contamination appeared to cause the samples to contract at progressively lower temperatures, with the

rapid contraction occurring at approximately 2200°F (1204°C), 2000°F (1093°C), and 1800°F (982°C) for the 0.84%, 1.78%, and 2.56% samples respectively. The sample with 2.56% quartz had a more severe expansion profile at lower temperature when compared to the other trials, and it maintained its peak expansion over a 400°F (204°C) temperature increase period.

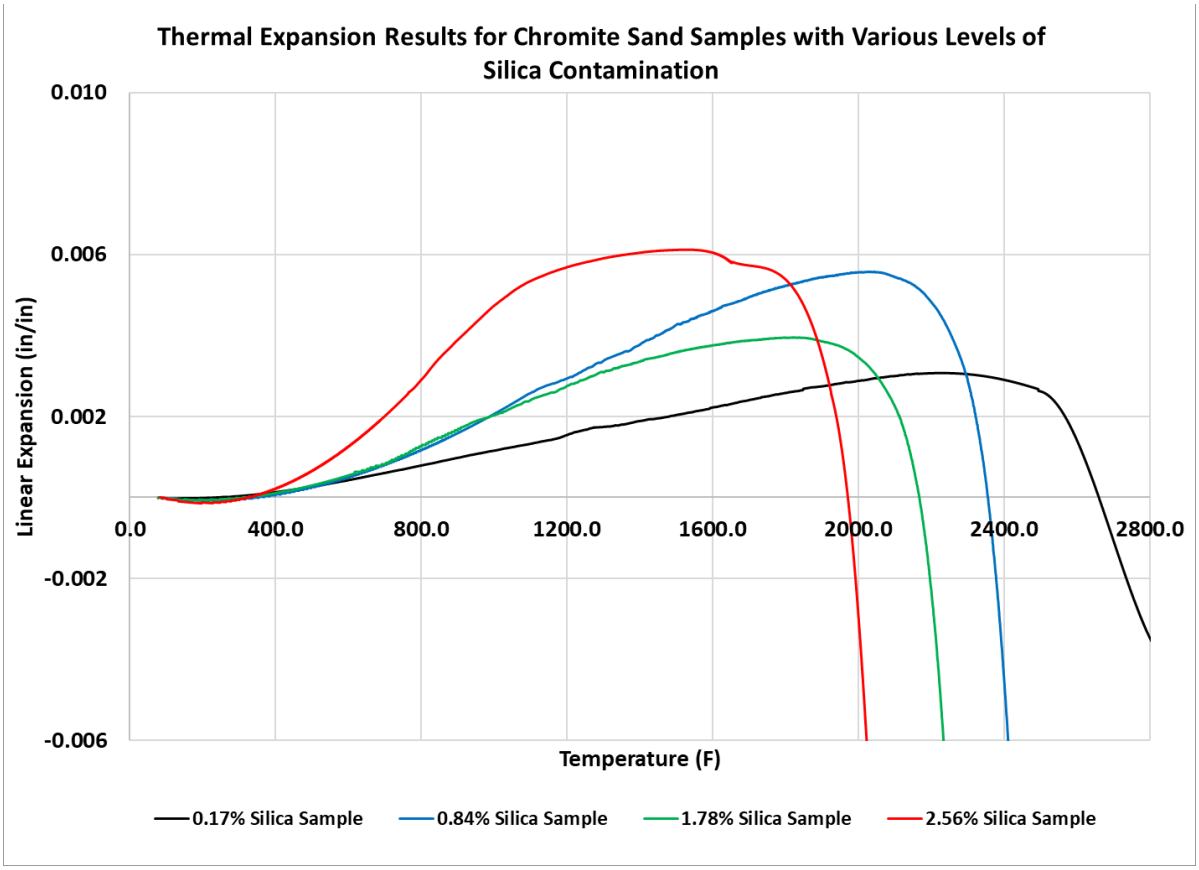

Figure 20: Dilatometry results for chromite samples with different concentrations of quartz.

Surface Viscosity and Associated Sinter Temperature Results

Using the data obtained from dilatometry, the surface viscosity was derived for each of the samples, as seen in Figure 21. There peaks present within the figure represent

the surface softening of the aggregate at the contact points, and it can be observed that increasing the quartz content in the samples caused this phenomena to occur at progressively lower temperatures. Specifically, the high-purity control sample containing 0.17% silica exhibited a sintering temperature of 2660°F (1460°C), and the sample containing 2.56% quartz sintered at 1969°F (1076°C).

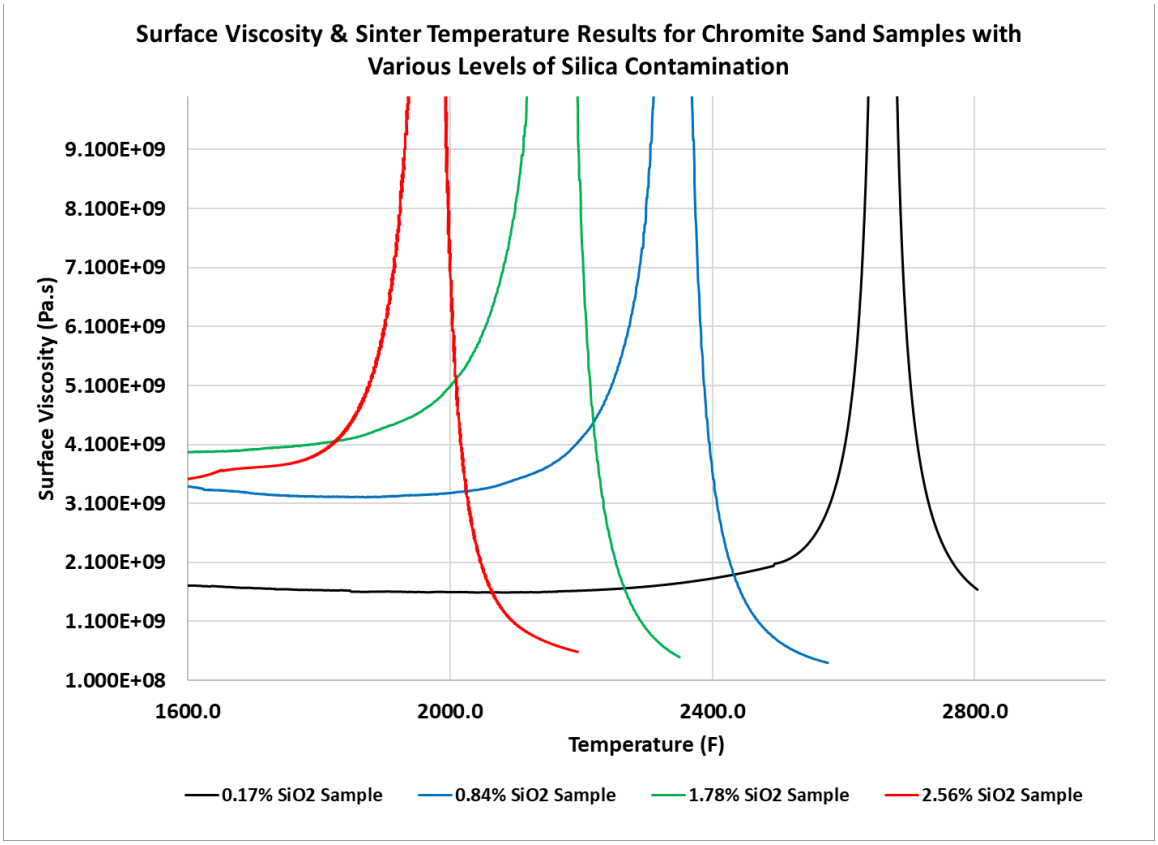

Figure 21: Surface viscosity and associated sinter temperature results for chromite samples.

The sinter temperature results were then plotted as a linear function of quartz concentration in Figure 22. Equations were provided for both imperial and metric systems, and a strong linear relationship is observed with a coefficient of determination of 0.9646. Reiterating, the sintering temperature of chromite sand was highly dependent

on the concentration of quartz within the system, and could attribute to the wide variability in performance characteristics between chromite distributors.

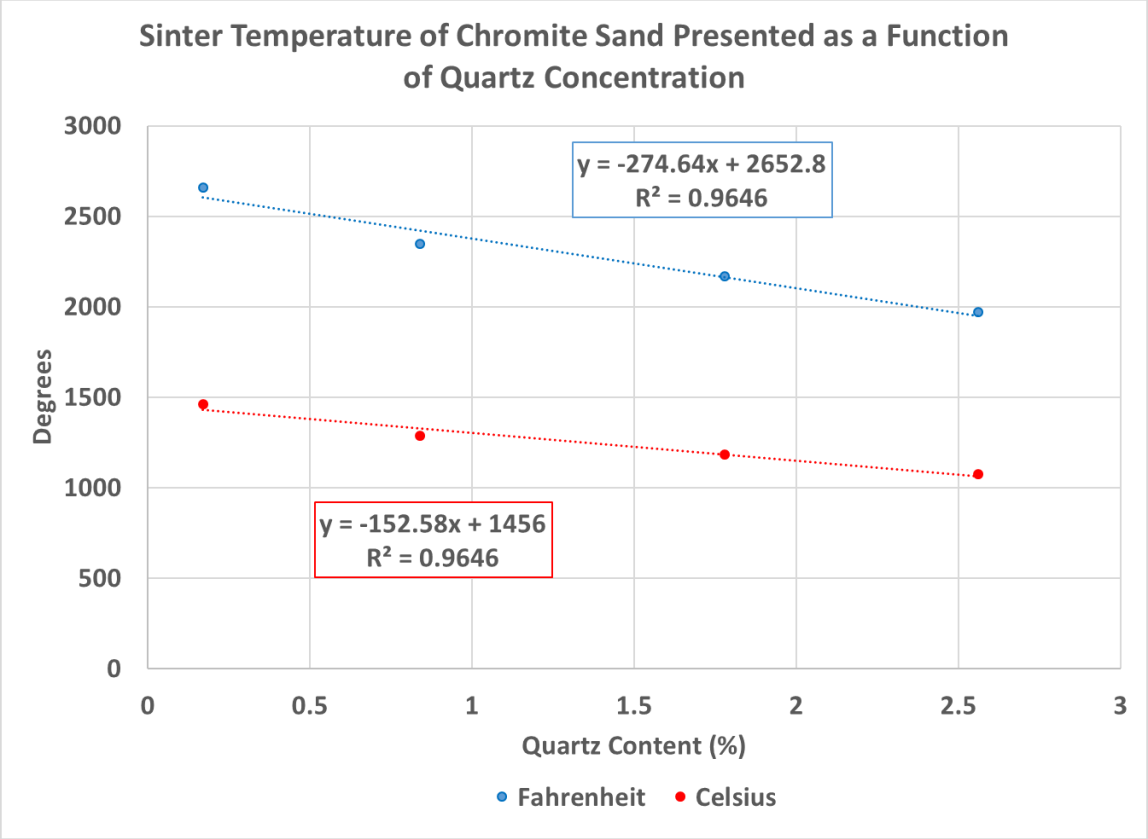

Figure 22: The relationship between sintering temperature and quartz content within chromite sand.

Presentation of Simulation Model Logic

Utilizing the data that was gathered throughout this investigation, two algorithms were developed to predict the formation and propensity of the double-skin penetration defect. Since double-skin penetration is often classified as a hybrid penetration defect, the two models will be used to determine the principle mechanism of its formation. The chemical mechanism algorithm is based entirely on the formation of fayalite, and the

mechanical mechanism algorithm utilizes the sintering temperature as its basis for calculation.

Chemical Penetration Mechanism Algorithm

The chemical mechanism algorithm logic is displayed as a flow diagram in Figure 23. Upon initializing the solidification simulation, the model checks if the sand cell surpasses 1434℃ (2613.3°F). This indicates that the mold atmosphere will be conducive to fayalite formation because the sand temperature surpasses the mathematically defined intersection temperature discovered in Figure 18 of this investigation. If the cell meets this condition, the cell is assigned an arbitrary value of "1" to indicate that this cell could produce fayalite, which can be used to understand what locations the defect is expected to occur. If the condition is unmet, the simulation is allowed to progress to the next time step, where the procedure is repeated for every sand cell until the simulation ends.

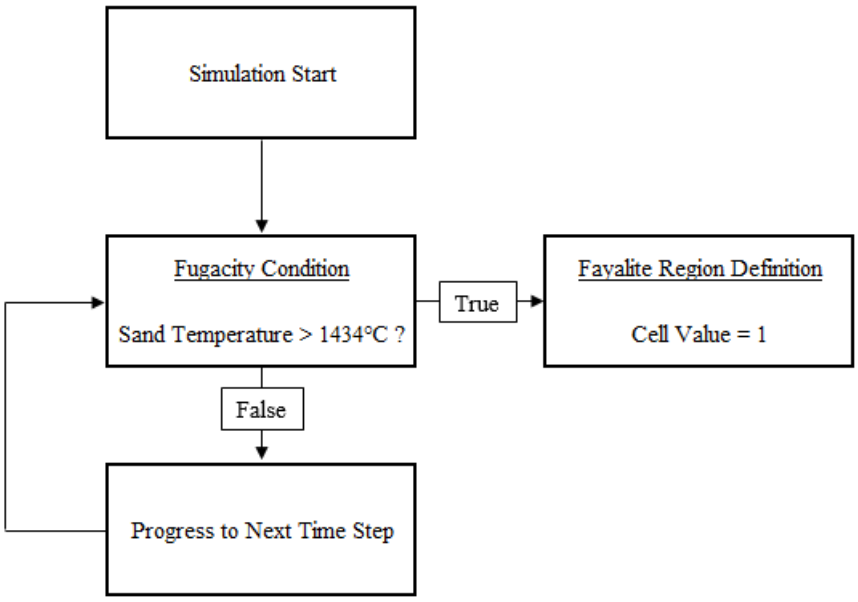

Figure 23: Flow diagram that illustrates the logical progression of the double-skin penetration prediction algorithm through the chemical mechanism.

Chemical Mechanism Algorithm Assumptions

The chemical mechanism model assumes that within each chromite sand cell there are sufficient wüstite-quartz interfaces for fayalite to form. This is assumed because there was no feasible way to identify how many interfaces are truly present in the system. Secondly, the model assumes that the liquid fayalite will overcome some critical liquid fraction or pressure yet to be determined for it to percolate throughout the isolated cell's theoretical interstices. Lastly, this model does not take into consideration the reaction kinetics involved in creating fayalite, as these considerations were not realized through this investigation.

Mechanical Penetration Mechanism Algorithm

Interestingly, fayalite is predicted to form at temperatures that are often higher than the sintering temperature of the chromite sand, which counters the initial hypothesis that fayalite formation causes the sand sinter temperature to decrease. The mechanical mechanism algorithm ignores the fugacity condition, and instead isolates the sinter temperature condition as seen in the logical flow diagram in Figure 24. When the simulation initializes, the temperature of the sand cells are compared to the sinter temperature at each time step. If the condition is true, the total time the sand surpassed the sinter temperature is calculated. If the condition is unmet, the simulation is allowed to progress to the next time step, where the procedure is repeated for every sand cell until the simulation ends.

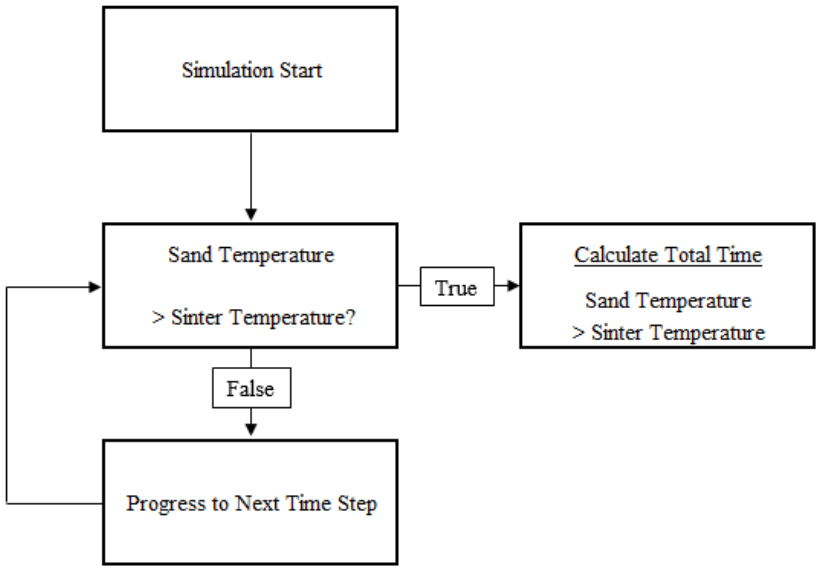

Figure 24: Flow diagram that illustrates the logical progression of the double-skin penetration prediction algorithm through the mechanical mechanism.

Mechanical Mechanism Algorithm Assumptions

The mechanical mechanism model assumes that the bulk chromite material exhibits identical sintering temperatures in each cell, which doesn't take into consideration the random distribution of particles in the aggregate. Also, since the model is based entirely on temperature, the metallostatic head pressure is assumed to be constant in this calculation. Due to limitations of the user result programming within MAGMASoft™, the solid fraction of the metal was unable to be used as a constraint within the mechanical model as well. This would prove useful to the model, as solid metal obviously cannot be drawn into the interstices of the metal. As a result, the model assumes that penetration is independent of the physical state of the cast metal.

Presentation of Demonstrative Model Results

In this example, the commercial steel casting geometry used to illustrate the double-skin penetration defect in Figure 1 will act as a demonstrative medium for the calculation results. The process and material variables were changed within the simulation to closely match what is used by the commercial foundry.

The chemical mechanism algorithm results are displayed in Figure 25. As seen within the figure, the highlighted cells indicate where fayalite is expected to form based upon the fugacity condition. The scale exhibits an absence of units, because the result is based on a binary scale where “1” indicates fayalite formation, and “0” predicts the opposite. This result shows some level of agreement with the commercial casting in select areas, but the model did not predict fayalite to form at the large mass present between the teeth.

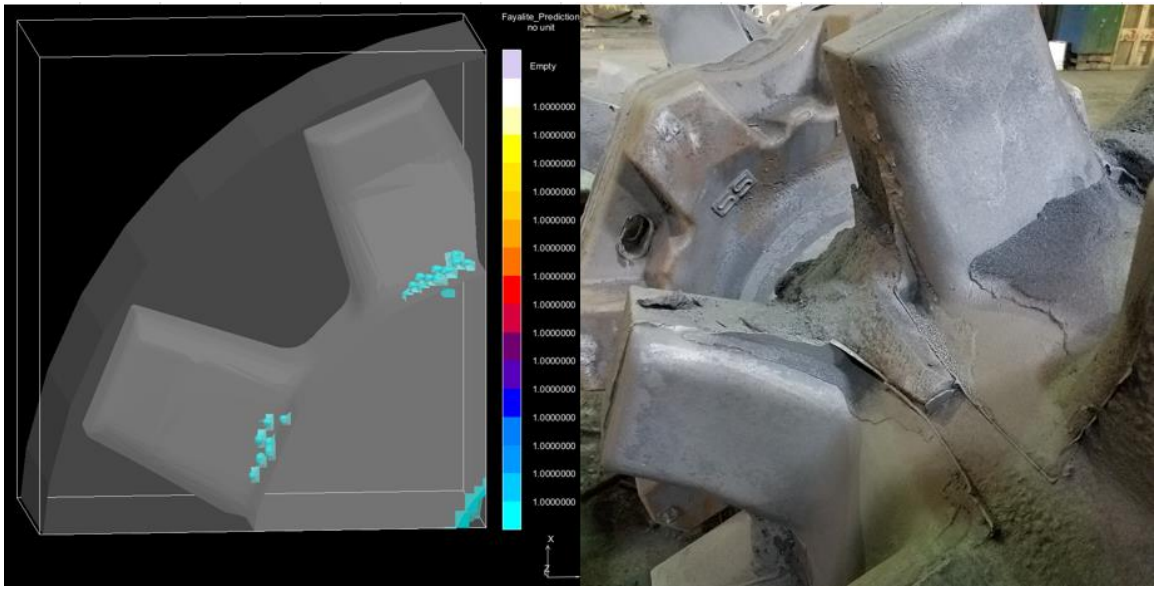

Figure 25: Comparison between chemical mechanism algorithm result and commercial casting defect.

The results for the mechanical mechanism algorithm are presented in Figure 26. The scale, which is provided in units of time (seconds), represents the cumulative time that each individual sand cell surpassed the associated sintering temperature, which in the case of this calculation, was 1358℃ (2476.4°F). The mechanical mechanism algorithm showed better agreement in the area between the teeth, unlike the first model. However, it seems that this algorithm predicted more penetration than what was observed on the production casting.

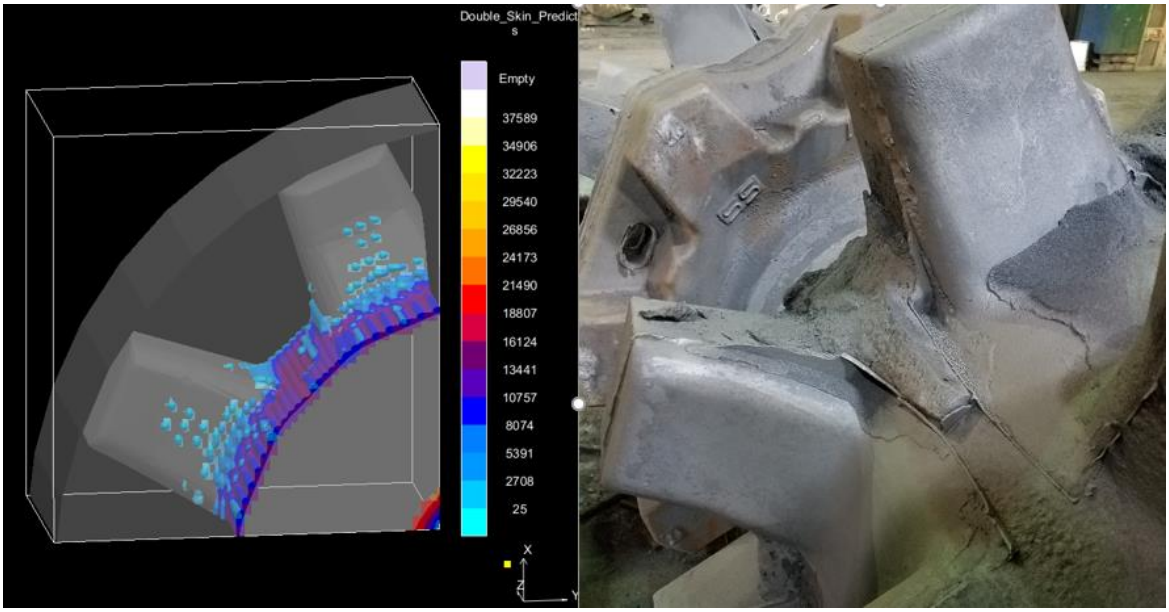

Figure 26: Comparison between mechanical mechanism algorithm result and commercial casting defect.

CHAPTER V

CONCLUSION AND RECOMMENDATIONS

When the results for the carbon monoxide and carbon dioxide emissions measurements during casting were compared to those seen in previous research by Barlow (1997), there was a strong agreement observed. This emissions data did indicate that while the overall concentrations of CO and CO_2 may change according to the quantity of ester-cured phenolic resin present within the mold, the ratio between the two stays relatively constant throughout the casting process. Interestingly, there was no observed double-skin penetration within the test casting. This may be due to a limitation regarding the nature of the experiment itself. The sampling probe drew evolved gas from the core at the aforementioned rate of 1 liter per minute, in turn possibly changing the overall susceptibility for penetration. The measured CO_2/CO ratio was able to be used to calculate the oxygen fugacity within the mold as a function of temperature, which allowed the comparison to the fayalite stability region defined by O'Neill (1987) to be possible. Although, the stated QFM and QFI equilibria within O'Neill's (1987) investigation were only defined within the temperature range of 626.85 – 1146.85℃ (1160 – 2096.3°F), and extrapolating that data to match temperatures associated with steel casting could be a dangerous assumption. If the region was fully explored, say to temperatures as high as 1600℃ (2912°F), the proposed model could be updated to be more representative of thermodynamic reality, thus increasing the accuracy of the algorithm.

It was concluded from the surface viscosity results that progressively higher concentrations of quartz within chromite sand had a strong correlation with decreasing sintering temperature. There was another observed correlation that showed a decrease in overall thermal stability when contaminated chromite sand was heated to elevated temperatures, which resembled data presented by Ravi (2018) It was originally hypothesized that fayalite formation caused the sintering temperature of chromite sand to progressively decrease, and increasing the quantity of quartz would assist in this phenomena. However, it was determined by the fugacity data that fayalite wouldn't form until the sand surpasses the intersection point defined by this investigation as 1434℃ (2613.3°F). This observation lead to two conclusions, one of which is that the oxygen fugacity may not be a sufficient explanatory variable to predict the formation of fayalite, or fayalite formation does not influence the sintering temperature of chromite sand.

Regardless, the two proposed models based on the principle penetration mechanisms both showed some level of agreeance with the production casting. The mechanical mechanism algorithm, however, predicted the defect more accurately than the chemical, which indicates that the mechanical penetration mechanism is the fundamental cause of double-skin penetration. Considering the fact that there was some overlap between the two models, it could be concluded that double-skin penetration is not solely formed through mechanical penetration, though. In fact, double-skin penetration could be the result of a cascading effect between both chemical and mechanical mechanisms, as shown by the demonstrative model results.

Through this investigation, several factors that contribute to double-skin penetration were realized, namely the level of silica contamination within the chromite sand, the section thickness of the casting, and the associated temperature. Knowing this, it is possible to reduce the risk of double-skin penetration by using a higher purity chromite sand with minute levels of quartz, changing the design of the casting to reduce heavy sections of steel, or by lowering the pouring temperature of the metal during the casting process. These conclusions about material and process changes are further supported by the proposed double-skin penetration prediction models.

In the future, it is recommended that the chemical mechanism model is updated to reflect the kinetics involved in the formation of fayalite. This could provide a more accurate depiction of the defect than the proposed model based on oxygen fugacity. However, if the proposed chemical mechanism model was to be further explored, it would prove valuable to collect temperature dependent carbon emissions data for more binder systems such as phenolic urethane, green sand, and sodium silicate, as the fugacity would drastically change according to Barlow's data. At the moment, the mechanical model predicts penetration if the sand cell surpasses the sintering temperature for any length of time. There is a possibility that there is a threshold time value for penetration to occur by means of the mechanical mechanism, and if that factor was realized, the model could be further constrained to compensate for this consideration.

REFERENCES

American Foundry Society. (2015). *AFS mold and core test handbook* (4th ed.). Schaumburg, IL: American Foundry Society.

Barlow, J.O., Owens, M., Stefanescu, D.M., Lane, A.M., & Piwonka, T.S. (1997). Chemical penetration in sand molds in steel castings. *AFS Transactions*, 325-331.

Bredt, J. (1995). *Binder stability and powder/binder interaction in three dimensional printing* (Doctoral Dissertation). Retrieved from http://hdl.handle.net/1721.1/10999

Bryant, N., & Thiel, J. (2017). Critical characteristics affecting the surface finish of castings. *AFS Transactions,* 303-311.

Draper, A.L., & Gaindhar, J.L. (1975). The role of mold atmospheres in the penetration of steel in sand molds. *AFS Transactions*, 593-615.

Fegley, B. (2012). *Practical chemical thermodynamics for geoscientists*. Cambridge, MA: Academic Press.

Fisler, D., & Mackwell, S. (1993). Kinetics of diffusion-controlled growth of fayalite. *Physics and Chemistry of Minerals,* 156-165.

Fukuyama, H., Donald, J., & Toguri, J. (1997).Wetting behavior between fayalite-type slags and solid magnesia. *Journal of the American Ceramic Society,* 2229-2236.

Giese, S.R., Stefanescu, D.M., Barlow, J., & Piwonka, T.S. (1997). Castiron penetration in sand molds: Part II. *AFS Transactions,* 1249-1257.

Gillson, J.L. (Ed.). (1971), *Industrial minerals and rocks,* (3rd ed.). New York, NY: American Institute of Mining, Metallurgical and Petroleum Engineers.

Hayes, K.D., Barlow, J.O., Stefanescu, D.M., & Piwonka, T.S. (1998). Mechanical penetration of liquid steel in sand molds. *AFS Transactions,* 769-776.

Jacob, K.T., Kale, G.M., & Iyengar, G.N.K. (1989). Chemical potentials of oxygen for fayalite-quartz-iron and fayalite-quartz-magnetite equilibria. *Metallurgical Transactions,* 679-685.

Liu, Y., & German, R. M. (1996). Contact angle and solid-liquid-vapor equilibrium. *Acta Materialia,* 1657-1663.

Luo, Y., Zhu, D., Zhou, X., & Zhang, F. (2015). Coproduction of DRI powder and semi-coke from siderite ore and low rank coal by excessive coal-based direct reduction in rotary kiln. *ISIJ International*, 78-87.

Luth, L. (2010). Chromite issues with large steel castings. *Steel Founders' Society of America Research Reports*.

McClellan, J., III., & Dorn, H. (2006). *Science and technology in world history: An introduction* (2nd ed.). Baltimore, MD: JHU Press.

Middleton, J.M. (1973). Tests and specifications for the control of molding materials. *The British Foundryman*, 258-267.

O'Neill, H. (1987). Quartz-fayalite-iron and quartz-fayalite-magnetite equilibria and the free energy of formation of fayalite (Fe_2SiO_4) and magnetite (Fe_3O_4). *American Mineralogist*, 67-75.

Pattabhi, R., Lane, A.M., & Piwonka, T.S. (1996). Cast iron penetration in sand molds: Part III. *AFS Transactions,* 1259-1268.

Ravi, S., Thiel, J., Bryant, N., Giese, S., & Schneiter, T. (2018). Use of dilatometry to evaluate the high temperature characteristics of silica in chromite sand. *International Journal of Metalcasting.*

Savage, R.E., & Taylor, H.F. (1950). A thermodynamic study of pinhole formation in steel castings. *AFS Transactions,* 564-577.

Scheffer, K.D., Sr. (1975). Behavior of chromite in steel casting molds and cores. *AFS Transactions,* 585-592.

Scott, W.D. (1993). Mineral separation in the steel foundry. *Proceedings of the 1st Cti Conference*.

Scott, W.D., Thomas, E.M., & Strohmayer, L.L. (2003.) Quality issues in the selection of chromite sand for steel foundry use. *AFS Transactions*, 517-527.

Shaw, T. (1986). Liquid redistribution during liquid-phase sintering. *Journal of the American Ceramic Society*, 27-34.

Steel Founders Society of America. (1967). *Tentative specification for chromite sand and flour*. Crystal Lake, IL: Steel Founders Society of America.

Stefanescu, D.M., Giese, S.R., Piwonka, T.S., & Lane, A.M. (1996). Cast iron penetration in sand molds: Part I. *AFS Transactions*, 1233-1248.

Stefanescu, D.M., Piwonka, T.S., Giese, S.R., and Lane, A.M. (1993). Metal penetration in sand molds: A fundamental approach to solving the problem. *AFS Transactions*, 789-796.

Tardos, G., Mazzone, D., & Pfeffer, R. (1984). Measurement of surface viscosities using a dilatometer. *The Canadian Journal of Chemical Engineering*, 884-888.

Thiel, J., & Ravi, S. (2014). Causes and solutions to veining defects in iron and steel castings. *AFS Transactions*, 171-186.

Toledo, M. (2002). *Analytical chemistry usercom* (7th ed.). Columbus, OH: Mettler Toledo.

Wilkinson, D., & Willemsen, J. (1983). Invasion percolation: A new form of percolation theory. *Journal of Physics A: Mathematics and General*, 3365-3376.